

# Randomized Preconditioned Solvers for Strong Constraint 4D-Var Data Assimilation

Amit N. Subrahmanya<sup>a</sup>, Vishwas Rao<sup>b</sup>, Arvind K. Saibaba<sup>c,\*</sup>

<sup>a</sup>*Computational Science Laboratory, Department of Computer Science, Virginia Tech, 620 Drillfield Dr., Blacksburg, 24061, VA, USA*

<sup>b</sup>*Argonne National Laboratory, 9700 S Cass Ave, Lemont, 60439, IL, USA*

<sup>c</sup>*Department of Mathematics, North Carolina State University, 2311 Stinson Dr., Raleigh, 27695, NC, USA*

---

## Abstract

Strong Constraint 4D Variational (SC-4DVAR) is a data assimilation method that is widely used in climate and weather applications. SC-4DVAR involves solving a minimization problem to compute the maximum a posteriori estimate, which we tackle using the Gauss-Newton method. The computation of the descent direction is expensive since it involves the solution of a large-scale and potentially ill-conditioned linear system, solved using the preconditioned conjugate gradient (PCG) method. To address this cost, we efficiently construct scalable preconditioners using three different randomization techniques, which all rely on a certain low-rank structure involving the Gauss-Newton Hessian. The proposed techniques come with theoretical (probabilistic) guarantees on the condition number, and at the same time, are amenable to parallelization. We also develop an adaptive approach to estimate the sketch size and to choose between the reuse or recomputation of the preconditioner. We demonstrate the performance and effectiveness of our methodology on two representative model problems—the Burgers and barotropic vorticity equation—showing a drastic reduction in both the number of PCG iterations and the number of Gauss-Newton Hessian products (after including the preconditioner construction cost).

*Keywords:* Variational data assimilation, randomized algorithms, preconditioned iterative methods, Gauss-Newton

---

## 1. Introduction

Data assimilation (DA), having origins in meteorology and oceanography, aims to optimally blend prior knowledge coming from a computational model of a dynamical system with noisy observations of reality to estimate the system states, parameters, or controls while quantifying the uncertainties of the said estimates [13, 2]. Data assimilation can be viewed in a Bayesian framework where the current best estimate is obtained from a posterior distribution that combines a prior distribution (of the previous best estimate) with observational likelihood [22]. The Strong Constraint 4D-Variational approach (SC-4DVAR), is a well-known DA framework used to estimate the initial condition of a system under a perfect model assumption. Essentially, the

---

\*Corresponding author

*Email addresses:* [amitns@vt.edu](mailto:amitns@vt.edu) (Amit N. Subrahmanya), [vhebbur@anl.gov](mailto:vhebbur@anl.gov) (Vishwas Rao), [asaibab@ncsu.edu](mailto:asaibab@ncsu.edu) (Arvind K. Saibaba)

SC-4DVAR discovers an optimal estimate of the initial condition that maximizes the Bayesian posterior probability over a spatiotemporal (hence, the name, 4D) trajectory consisting of background, observation, and model information [23]. Typically, the SC-4DVAR optimization problem [13] is solved using Newton-based methods such as the Gauss-Newton (GN) approach [27, 6]. Problems with fine-scale discretization, require the solution of a large linear system to compute the Gauss-Newton descent direction. Iterative linear solvers are typically used since they require matrix-vector products rather than matrix decompositions, making them memory efficient. In this work, we use the preconditioned conjugate gradient (PCG) method [31], requiring the actions of the tangent linear model (TLM) and adjoint model (ADJ) [22, 13]. The performance of PCG depends crucially on the use of a good preconditioner, which is the central focus of this paper.

In recent years, randomized methods have emerged as a powerful tool in scientific computing for accelerating expensive computations (see, e.g., recent surveys [20, 24]). Randomized methods have strong theoretical guarantees, reduced computational costs, and are highly parallelizable. A key ingredient in the randomized methods is the use of a sketch of the matrix of interest (obtained by computing the product of the matrix with an appropriately chosen random matrix) which captures the desired essential features of the matrix. Randomization for least-squares problems roughly comes in two flavors: sketch and solve, or sketch and precondition. In the sketch and solve approach, randomization is used as a dimensionality reduction tool to solve a smaller inexact problem, whereas in the sketch and precondition approach, randomization is used to accelerate the convergence of the PCG method.

*Contributions.* This paper proposes multiple, efficient, randomized solvers for SC-4DVAR. Our contributions are subdivided into three parts—algorithms, analysis, and numerical experiments.

1. **Algorithms:** The eigenvalues of the data-misfit part of the GN Hessian (previously analyzed by [14, 5, 37, 8]), when preconditioned by the background covariance, exhibit rapid decay. We exploit this fact to propose three different randomized algorithms (i) Randomized SVD (RandSVD), (ii) Nyström, and (iii) Single View (SingleView), to compute a low-rank sketch of the GN Hessian for SC-4DVAR, and demonstrate the reliability of its low-rank sketch, both in theory and practice. These three sketching methods can be used in the following ways:
  - (a) **SketchSolv:** The GN descent direction is obtained by multiplying the inverse of the low-rank sketch with the gradient to obtain a descent direction.
  - (b) **SketchPrec:** The GN descent direction is obtained by using the GN Hessian in PCG preconditioned by the inverse of the low-rank sketch. We also develop an adaptive preconditioning, adaptive sketching approach based on RandSVD that decides (1) when to recompute the preconditioner and (2) the sketch size of the low-rank approximation that is used to compute the preconditioner.

The first two randomized methods (RandSVD, Nyström) are nearly identical in cost, error, and performance. The third method (SingleView), while more expensive to compute, offers an additional level of parallelism.

2. **Analysis:** A twofold analysis—*structural*, and *probabilistic*—of the proposed sketching methods is presented in this paper.

- (a) **Structural analysis:** We analyze the performance of the approximation for a single step of the Gauss-Newton iteration in three metrics: relative error in the inverse, the error in the solution, and the condition number of the preconditioned operator of the GN iterations. The analysis is applicable beyond low-rank approximations and the randomized algorithms proposed in this paper.
- (b) **Probabilistic analysis:** We develop specific analyses for the three randomized methods in expectation. The bounds do not show explicit dependence on the size of the matrices and provide insight into the sampling parameters.

3. **Numerical Experiments:** We validate the proposed methods on two challenging model problems: 1D Burgers equations, and the barotropic-vorticity equation.

Our experiments show that the randomized sketching methods result in (i) faster convergence of PCG measured in the number of iterations, (ii) reduction in the total number of TLM and ADJ evaluations, and at the same time, (iii) parallel evaluation of multiple batches of TLM and ADJ vector products. For the Burgers equation, we also investigate (i) the number of random vectors necessary to obtain a good preconditioner, (ii) the influence of diffusion and problem mesh size on the conditioning of the GN Hessian matrix and its relative spectral decay, and (iii) the effect of changing the mesh size on PCG iterations. Our recommendation based on the experiments is to use RandSVD\_Adapt, since this uses fewer TLM and ADJ evaluations than SketchPrec and standard Gauss-Newton methods, even after accounting for the cost of constructing the preconditioners. At the same time, we do not prefer the SketchSolv method over SketchPrec due to its inherent inexactness.

*Literature review.* Randomization has applications in accelerating computations in Bayesian inverse problems in several ways. Firstly, it has been used to accelerate optimization by using randomized approximations of the cost function, such as the stochastic and sample average approximation methods in [26]. Secondly, randomization is used in inverse problems to approximate the posterior covariance through a low-rank approximation of the prior-preconditioned data-misfit part of the Hessian [43, 32]. Third, it has been used to reduce the number of PDE solves in Bayesian inference [33]. The randomized approaches used here also target the optimization problem of computing the MAP estimate, but use the same idea of low-rank approximation used to approximate the posterior covariance.

There is a long history of preconditioning iterative methods in the context of data assimilation, see [16] for some key references. However, to our knowledge, there exists limited work and analysis on methods that combine randomization with SC-4DVar. In [10], the authors consider the forcing formulation of the weak-constraint 4D-Var (WC-4DVAR), with a Nyström as a preconditioner for PCG iterations. The previous ideas are extended to a state formulation of the incremental WC-4DVAR in [9] that allows for parallelism in time. We note that the analysis is related to [15] (note that this is not in the context of DA applications) but is more general since our analysis applies to a general covariance matrix and is not necessarily restricted to a scaled identity matrix. Additionally, while [15] focuses on the Nyström approximation, we also present and analyze algorithms for RandSVD and SingleView. The paper [4] presents an approach that uses RandSVD to approximate the inverse of the Hessian to directly compute the descent direction for incremental 4D-Var. Another interesting paper [17] presents low-rank preconditioners with GMRES to solve weak constraint 4D-Var. We believe our formulation, while done for SC-4DVAR, can be extended to the weak constraint and incremental variants.

## 2. Background

### 2.1. Data Assimilation

As stated in the introduction, data assimilation for state estimation combines information from three different sources: the prior best estimate, the model dynamics, and observations, to produce an improved estimate of the true state. Formally, let us denote the unknown true state at time  $t_0$  as  $\mathbf{x}_0^{\text{true}} \in \mathbb{R}^n$  and the prior best estimate, called the background, by  $\mathbf{x}_0^b \in \mathbb{R}^n$ . The computational model—here, a set of differential equations—which evolves an initial state  $\mathbf{x}_0 \in \mathbb{R}^n$  at time  $t_0$  to future state  $\mathbf{x}_i \in \mathbb{R}^n$ , is denoted by

$$\mathbf{x}_i = \mathcal{M}_{t_0 \rightarrow t_i}(\mathbf{x}_0), \text{ where } \mathcal{M}_{t_0 \rightarrow t_i} : \mathbb{R}^n \rightarrow \mathbb{R}^n, 1 \leq i \leq n_t. \quad (1)$$

Typically, this model is assumed inadequate, due to unknown dynamics, computational approximations, random errors, and so on. Observations are expensive to obtain because only a limited number of sensors can be used to collect data and are typically much smaller than the discretization of the system state, and at the same time are imperfect due to measurement errors. This makes the problem of estimating the initial conditions  $\mathbf{x}_0$  an ill-posed problem. Specifically, the observations  $\mathbf{y}_i \in \mathbb{R}^{n_{\text{obs}}}$  of the physical state are taken at times  $t_i$ ,  $1 \leq i \leq n_t$  as

$$\mathbf{y}_i = \mathcal{O}(\mathbf{x}_i^{\text{true}}) + \boldsymbol{\varepsilon}_i^{\text{obs}}, \text{ where } \mathcal{O} : \mathbb{R}^n \rightarrow \mathbb{R}^{n_{\text{obs}}} \text{ and } n_{\text{obs}} \ll n. \quad (2)$$

Here,  $\mathcal{O}$  is the observation operator and  $\boldsymbol{\varepsilon}_i^{\text{obs}}$  represents observation error. As is the typical case, observation errors at different times are assumed to be conditionally independent [13]. From a Bayesian standpoint, we define the posterior distribution given the observational likelihood, model evolution likelihood, and the prior as:

$$\pi(\mathbf{x}_0 | \mathbf{y}_1, \dots, \mathbf{y}_{n_t}) \propto \pi(\mathbf{x}_0) \left( \prod_{i=1}^{n_t} \pi(\mathbf{y}_i | \mathbf{x}_i) \pi(\mathbf{x}_i | \mathbf{x}_{i-1}) \right). \quad (3)$$

SC-4DVAR makes certain assumptions about the model, prior, and observational likelihoods. The first assumption is that the prior and likelihoods are normally distributed, i.e.,  $\mathbf{x}_0 \sim \mathcal{N}(\mathbf{x}_0^b, \boldsymbol{\Gamma})$  and  $\boldsymbol{\varepsilon}_i^{\text{obs}} \sim \mathcal{N}(\mathbf{0}, \mathbf{R}_i)$  and the measurements are uncorrelated in time. The next assumption is that of a deterministic model with no model error, implying that  $\pi(\mathbf{x}_i | \mathbf{x}_{i-1}) = 1$ . With these simplifying assumptions, the posterior distribution takes the form

$$\begin{aligned} \pi(\mathbf{x}_0 | \mathbf{y}_1, \dots, \mathbf{y}_{n_t}) \propto & \exp\left(-\frac{1}{2} (\mathbf{x}_0 - \mathbf{x}_0^b)^\top \boldsymbol{\Gamma}^{-1} (\mathbf{x}_0 - \mathbf{x}_0^b)\right) \\ & \times \exp\left(-\frac{1}{2} \sum_{i=1}^{n_t} (\mathcal{O}(\mathbf{x}_i) - \mathbf{y}_i)^\top \mathbf{R}_i^{-1} (\mathcal{O}(\mathbf{x}_i) - \mathbf{y}_i)\right). \end{aligned} \quad (4)$$

SC-4DVAR computes the maximum a posteriori (MAP) estimate  $\mathbf{x}_0^a$  by solving the following optimization problem:

$$\mathbf{x}_0^a \in \arg \min_{\mathbf{x}_0 \in \mathbb{R}^n} \mathcal{J}(\mathbf{x}_0) \quad \text{subject to: } \mathbf{x}_i = \mathcal{M}_{t_0 \rightarrow t_i}(\mathbf{x}_0), \quad 1 \leq i \leq n_t, \quad (5)$$

where the objective function is defined to be the negative logarithm of the posterior distribution (ignoring the proportionality constant which does not affect the optimal point  $\mathbf{x}_0^a$ )

$$\begin{aligned} \mathcal{J}(\mathbf{x}_0) = -\log \pi(\mathbf{x}_0 | \mathbf{y}_1, \dots, \mathbf{y}_{n_t}) = & \frac{1}{2} (\mathbf{x}_0 - \mathbf{x}_0^b)^\top \boldsymbol{\Gamma}^{-1} (\mathbf{x}_0 - \mathbf{x}_0^b) \\ & + \frac{1}{2} \sum_{i=1}^{n_t} (\mathcal{O}(\mathbf{x}_i) - \mathbf{y}_i)^\top \mathbf{R}_i^{-1} (\mathcal{O}(\mathbf{x}_i) - \mathbf{y}_i). \end{aligned} \quad (6)$$

The first term in eq. (6) quantifies the departure of the solution from the background state  $\mathbf{x}_0^b$  and the second term measures the mismatch between the forecast trajectory and observations in the assimilation window. The minimizer of eq. (5) is typically computed iteratively using gradient-based numerical optimization methods. First-order adjoint models provide the gradient of the cost function eq. (6), while second-order adjoint models provide the Hessian-vector product (e.g., for Newton-type methods). The methodology for building and using various adjoint models for optimization and sensitivity analysis is discussed in [7, 36]. In this paper, we specifically consider the approach in [36] for constructing discrete Runge-Kutta adjoints.

## 2.2. Newton-based approaches

In this work, we focus on the GN method [27, 6] for two main reasons (i) it is cheaper than the full Newton method as it does not require the computation of second-order derivatives of the model, (ii) it is better suited for small residual problems and is robust to the initial guess for the optimization problem in (5). The gradient of eq. (6) can be written as

$$\nabla_{\mathbf{x}_0} \mathcal{J}(\mathbf{x}_0) = \mathbf{\Gamma}^{-1} \left( \mathbf{x}_0 - \mathbf{x}_0^b \right) + \sum_{i=1}^{n_t} \mathbf{M}_i^\top(\mathbf{x}_0) \mathbf{O}_i^\top(\mathbf{x}_i) \mathbf{R}_i^{-1} (\mathcal{O}(\mathbf{x}_i) - \mathbf{y}_i), \quad (7)$$

where  $\mathbf{M}_i^\top(\mathbf{x}_0) = \left. \frac{\partial \mathcal{M}_{t_0 \rightarrow t_i}^\top}{\partial \mathbf{x}} \right|_{\mathbf{x}_0}$  and  $\mathbf{O}_i^\top(\mathbf{x}_i) = \left. \frac{\partial \mathcal{O}^\top}{\partial \mathbf{x}} \right|_{\mathbf{x}_i}$  are the ADJs of the model and observation operators respectively. The GN Hessian of eq. (6) with respect to  $\mathbf{x}_0$  is

$$\mathcal{H}(\mathbf{x}_0) = \mathbf{\Gamma}^{-1} + \sum_{i=1}^{n_t} \mathbf{M}_i^\top(\mathbf{x}_0) \mathbf{O}_i^\top(\mathbf{x}_i) \mathbf{R}_i^{-1} \mathbf{O}_i(\mathbf{x}_i) \mathbf{M}_i(\mathbf{x}_0). \quad (8)$$

where  $\mathbf{M}_i(\mathbf{x}_0) = \left. \frac{\partial \mathcal{M}_{t_0 \rightarrow t_i}}{\partial \mathbf{x}} \right|_{\mathbf{x}_0}$  and  $\mathbf{O}_i(\mathbf{x}_i) = \left. \frac{\partial \mathcal{O}}{\partial \mathbf{x}} \right|_{\mathbf{x}_i}$  are the TLMs of the model and observation operators respectively. The GN Hessian is rewritten as  $\mathcal{H}(\mathbf{x}_0) = \mathbf{\Gamma}^{-1} + \mathbf{G}^\top(\mathbf{x}_0) \mathbf{G}(\mathbf{x}_0)$  where

$$\mathbf{G}(\mathbf{x}_0) = \begin{bmatrix} \mathbf{R}_1^{-1/2} \mathbf{O}_1(\mathbf{x}_1) \mathbf{M}_1(\mathbf{x}_0) \\ \mathbf{R}_2^{-1/2} \mathbf{O}_2(\mathbf{x}_2) \mathbf{M}_2(\mathbf{x}_0) \\ \vdots \\ \mathbf{R}_{n_t}^{-1/2} \mathbf{O}_{n_t}(\mathbf{x}_{n_t}) \mathbf{M}_{n_t}(\mathbf{x}_0) \end{bmatrix} \in \mathbb{R}^{m \times n}, \quad m = n_{\text{obs}} n_t. \quad (9)$$

An evaluation of the gradient involves a sequential computation of the full model forward in time and the adjoint model backward in time, while an evaluation of the GN Hessian requires a solution of the full model and its tangent linear model forward in time and the adjoint model backward in time.

As the minimization proceeds in the GN approach, we generate a sequence of iterates  $\mathbf{x}_0^{(k)}$ . At the current iterate, to obtain the GN descent direction  $\delta \mathbf{x}^{(k)}$ , we must solve the linear system

$$\mathcal{H}^{(k)} \delta \mathbf{x}^{(k)} = -\mathbf{g}^{(k)}, \quad (10)$$

where  $\mathcal{H}^{(k)} = \mathbf{\Gamma}^{-1} + \mathbf{G}^\top(k) \mathbf{G}^{(k)}$  is the GN Hessian (we write  $\mathbf{G}^{(k)} = \mathbf{G}(\mathbf{x}_0^{(k)})$  for short) and  $\mathbf{g}^{(k)} = \nabla_{\mathbf{x}_0} \mathcal{J}(\mathbf{x}_0^{(k)})$  is the gradient at the current iteration  $\mathbf{x}_0^{(k)}$ . We denote the data-misfit part of the Hessian  $\mathbf{H}^{(k)} = \mathbf{\Gamma}^{1/2} \mathbf{G}^\top(k) \mathbf{G}^{(k)} \mathbf{\Gamma}^{1/2}$  and re-write the Hessian as  $\mathcal{H}^{(k)} = \mathbf{\Gamma}^{-1/2} (\mathbf{I} + \mathbf{H}^{(k)}) \mathbf{\Gamma}^{-1/2}$ .

The main idea behind the approaches that we propose in the next sections is to generate an approximation to the GN Hessian. Suppose we have a low-rank approximation of the prior-preconditioned data-misfit part of the Hessian  $\mathbf{H}^{(k)} \approx \widehat{\mathbf{H}}^{(k)}$ , then, the GN Hessian can be approximated as  $\mathcal{H}^{(k)} \approx \widehat{\mathcal{H}}^{(k)} \equiv \mathbf{\Gamma}^{-1/2}(\mathbf{I} + \widehat{\mathbf{H}}^{(k)})\mathbf{\Gamma}^{-1/2}$ . To this end, we discuss several randomized algorithms to generate low-rank approximations  $\widehat{\mathbf{H}}^{(k)}$ .

### 3. Randomized Algorithms

In this section, we discuss different randomized methods for sketching the GN Hessian, and its application to the linear system in eq. (10). In Section 3.1, we discuss three methods to sketch  $\widehat{\mathbf{H}}^{(k)}$ , and then, in Section 3.2, we discuss two different ways to use it in eq. (10).

#### 3.1. Sketching the GN Hessian

As we discuss methods (RandSVD, Nyström, SingleView) to approximate the GN Hessian for a single step of an optimization iterate, we drop the dependence on the iterate ( $k$ ) to make the notation simpler. Let the current iterate be  $\mathbf{x} \in \mathbb{R}^n$  and define the preconditioned forward operator  $\mathbf{A} = \mathbf{G}\mathbf{\Gamma}^{1/2}$ , its adjoint  $\mathbf{A}^\top$  and the GN Hessian  $\mathcal{H}$ . An input to all sketches is a tunable sampling parameter  $\ell = r + p$  where  $r$  is the target rank for the sketch and  $p$  is some oversampling (typically, taken 10 – 20). The three methods presented here, perform a post-processing step to obtain a low-rank approximation of  $\widehat{\mathcal{H}} = \widehat{\mathbf{V}}\widehat{\mathbf{\Lambda}}\widehat{\mathbf{V}}^\top$ , where  $\widehat{\mathbf{V}} \in \mathbb{R}^{n \times \ell}$  has orthonormal columns, and  $\widehat{\mathbf{\Lambda}} \in \mathbb{R}^{\ell \times \ell}$  has nonnegative diagonal entries. This way,  $\widehat{\mathcal{H}}$  can be inverted using the Woodbury identity as

$$\widehat{\mathcal{H}}^{-1} = \mathbf{\Gamma}^{1/2}(\mathbf{I} + \widehat{\mathbf{V}}\widehat{\mathbf{\Lambda}}\widehat{\mathbf{V}}^\top)^{-1}\mathbf{\Gamma}^{1/2} = \mathbf{\Gamma}^{1/2} \left( \mathbf{I} - \widehat{\mathbf{V}}(\widehat{\mathbf{\Lambda}}^{-1} + \widehat{\mathbf{I}})^{-1}\widehat{\mathbf{V}}^\top \right) \mathbf{\Gamma}^{1/2}. \quad (11)$$

However, the postprocessing step is not always necessary to obtain a sketch (RandSVD and SingleView). The choice of  $\ell$  can be *fixed* or *adaptive* based on the specific application. In section 4.2, we show that for many problems of interest, as  $\mathcal{H}$  will have a spectrum with many small singular values, allowing the choice of  $\ell \ll m$ .

##### 3.1.1. Fixed-rank sketching

We now discuss three randomized methods to sketch the GN Hessian with a fixed sketch size.

*Randomized SVD.* Here, we compute a low-rank approximation of the preconditioned forward operator  $\mathbf{A}$  using the randomized SVD approach in [20]. First, we draw a random matrix  $\mathbf{\Omega} \in \mathbb{R}^{n \times \ell}$ .

Throughout this paper, we will assume that the random matrices are standard Gaussian, meaning that the entries are independent and identically distributed random variables drawn from the Gaussian distribution with zero mean and unit variance. Next, we compute the sketch  $\mathbf{Y} = \mathbf{A}\mathbf{\Omega}$ ; the key insight is that if  $\mathbf{A}$  is low-rank, then the columns of  $\mathbf{Y}$  approximate the range of  $\mathbf{A}$ . To obtain a low-rank approximation, we consider the thin-QR factorization  $\mathbf{Y} = \mathbf{Q}\mathbf{R}$  then obtain the low-rank approximation  $\mathbf{A} \approx \mathbf{Q}\mathbf{Q}^\top\mathbf{A}$ ; similarly, we also have the low-rank approximation

$$\mathbf{H} = \mathbf{A}^\top\mathbf{A} \approx \widehat{\mathbf{H}} \equiv \mathbf{A}^\top\mathbf{Q}\mathbf{Q}^\top\mathbf{A} = \mathbf{W}^\top\mathbf{W} \quad (12)$$

where  $\mathbf{W}^\top = \mathbf{A}^\top \mathbf{Q}$ . This approach requires  $\ell$  TLM applications followed by  $\ell$  ADJ applications—both of which can be computed in parallel. The computation of the QR factorization is  $\mathcal{O}(mr^2)$  floating point operations (flops), and there is an additional postprocessing cost  $\mathcal{O}(nr^2 + r^3)$  flops to convert to SVD format. The details of this approach are given in Algorithm 1.

---

**Algorithm 1** RandSVD GN Hessian Approximation

---

**Require:** Operator:  $\mathbf{A} \in \mathbb{R}^{m \times n}$ , sketch parameter:  $\ell$ .

- 1: Draw Gaussian random matrix  $\mathbf{\Omega} \in \mathbb{R}^{n \times \ell}$ .
  - 2: Compute forward pass  $\mathbf{Y} = \mathbf{A}\mathbf{\Omega}$ . {Compute, if possible, in parallel}
  - 3: Compute thin-QR factorization  $\mathbf{Y} = \mathbf{Q}\mathbf{R}$ .
  - 4: Compute  $\mathbf{W}^\top = \mathbf{A}^\top \mathbf{Q}$ . {Compute, if possible, in parallel}
  - 5: Compute thin-SVD  $\mathbf{W} = \widehat{\mathbf{U}}\widehat{\mathbf{\Sigma}}\widehat{\mathbf{V}}^\top$ ,  $\widehat{\mathbf{\Lambda}} = \widehat{\mathbf{\Sigma}}^2$ .
  - 6: **return** Matrices  $\widehat{\mathbf{V}}, \widehat{\mathbf{\Lambda}}$  that defines the approximation  $\widehat{\mathbf{H}} = \widehat{\mathbf{V}}\widehat{\mathbf{\Lambda}}\widehat{\mathbf{V}}^\top$ .
- 

*Nyström.* In this approach, we first form the sketch of the prior preconditioned GN Hessian,  $\mathbf{H}$ , by drawing a standard Gaussian random matrix  $\mathbf{\Omega} \in \mathbb{R}^{n \times \ell}$  and computing  $\mathbf{Y} = \mathbf{H}\mathbf{\Omega}$ . Notice that it requires  $\ell$  TLM followed by  $\ell$  adjoint solves which can be done in parallel. The Nyström approach forms the following low-rank approximation to  $\mathbf{H}$  as

$$\mathbf{H} \approx \mathbf{H}_{\text{Nys}} \equiv \mathbf{Y}(\mathbf{\Omega}^\top \mathbf{Y})^\dagger \mathbf{Y}^\top = \mathbf{H}\mathbf{\Omega}(\mathbf{\Omega}^\top \mathbf{H}\mathbf{\Omega})^\dagger (\mathbf{H}\mathbf{\Omega})^\top, \quad (13)$$

where  $\dagger$  represents the Moore-Penrose pseudo-inverse. However, the expression implemented *as is* has numerical instability issues, so we follow the approach in [41, Algorithm 3] – which is reproduced in Algorithm 2. The computational cost of the Nyström approach is similar to RandSVD; namely,  $\ell$  TLM followed by  $\ell$  ADJ solves followed by  $\mathcal{O}(r^2n + r^3)$  flops for post-processing.

---

**Algorithm 2** Nyström GN Hessian Approximation

---

**Require:** Operator:  $\mathbf{H} = \mathbf{A}^\top \mathbf{A} \in \mathbb{R}^{n \times n}$ , sketch parameter:  $\ell$ .

- 1: Draw Gaussian random matrix  $\mathbf{\Omega} \in \mathbb{R}^{n \times \ell}$
  - 2: Compute  $\mathbf{Y} = \mathbf{H}\mathbf{\Omega}$  {Compute, if possible, in parallel.}
  - 3: Compute  $\nu = \sqrt{n}\epsilon_{\text{mach}}\|\mathbf{Y}\|_2$  where  $\epsilon_{\text{mach}}$  is machine epsilon
  - 4:  $\mathbf{Y} \leftarrow \mathbf{Y} + \nu\mathbf{\Omega}$
  - 5: Compute (lower) Chokesky triangular factor  $\mathbf{L}$  of  $(\mathbf{C} + \mathbf{C}^\top)/2$ , where  $\mathbf{C} = \mathbf{\Omega}^\top \mathbf{Y}$
  - 6: Compute the thin-SVD (truncated to rank  $r$ ) of  $\mathbf{W}$  defined as  $\mathbf{L}^{-1}\mathbf{Y}^\top = \mathbf{W} = \widehat{\mathbf{U}}\widehat{\mathbf{\Sigma}}\widehat{\mathbf{V}}^\top$ .
  - 7: **return** Matrices  $\widehat{\mathbf{V}}, \widehat{\mathbf{\Lambda}} = \max\{0, \widehat{\mathbf{\Sigma}}^2 - \nu\mathbf{I}\}$  that defines the approximation  $\widehat{\mathbf{H}} = \widehat{\mathbf{V}}\widehat{\mathbf{\Lambda}}\widehat{\mathbf{V}}^\top$
- 

*Single View.* In this approach, we draw two standard Gaussian random matrices  $\mathbf{\Omega} \in \mathbb{R}^{n \times \ell_1}$ ,  $\mathbf{\Psi} \in \mathbb{R}^{m \times \ell_2}$ ; the sketch parameters  $\ell_1, \ell_2$  will be discussed shortly. As in RandSVD, we compute the sketch  $\mathbf{Y} = \mathbf{A}\mathbf{\Omega}$  and its thin-QR factorization  $\mathbf{Y} = \mathbf{Q}_Y \mathbf{R}_Y$ . The SingleView method maintains a separate sketch for the row space  $\mathbf{Z} = \mathbf{A}^\top \mathbf{\Psi}$ , and constructs the low-rank approximation

$$\mathbf{A} \approx \widehat{\mathbf{A}}_{SV} \equiv \mathbf{Q}_Y (\mathbf{\Psi}^\top \mathbf{Q}_Y)^\dagger \mathbf{Z}^\top. \quad (14)$$

A main advantage of this approach is that both the sketches  $\mathbf{Y}$  and  $\mathbf{Z}$  can be computed independently and in parallel. To understand this approach it is worth noting that the SingleView

approximation can be expressed as  $\widehat{\mathbf{A}}_{SV} \equiv \mathbf{P}_{SV} \mathbf{A}$ , where  $\mathbf{P}_{SV} = \mathbf{Q}_Y (\boldsymbol{\Psi}^\top \mathbf{Q}_Y)^\dagger \boldsymbol{\Psi}^\top$  is an oblique projector with  $\mathcal{R}(\mathbf{P}_{SV}) \subset \mathcal{R}(\mathbf{Q}_Y)$ . In contrast, the RandSVD approach uses an orthogonal projector onto  $\mathcal{R}(\mathbf{Q}_Y)$ . We now discuss an efficient implementation of the low-rank approximation.

Compute  $\mathbf{M} = \boldsymbol{\Psi}^\top \mathbf{Q}_Y$  and its thin-QR factorization  $\mathbf{M} = \mathbf{Q}_M \mathbf{R}_M$ ; its pseudoinverse can be computed as  $\mathbf{M}^\dagger = \mathbf{R}_M^\dagger \mathbf{Q}_M^\top$ . Now, we compute  $\mathbf{W} = \mathbf{R}_M^\dagger (\mathbf{Z} \mathbf{Q}_M)^\top$  and its thin-SVD  $\mathbf{W} = \mathbf{U}_W \boldsymbol{\Sigma} \widehat{\mathbf{V}}^\top$ . In summary, so far we have  $\mathbf{A}_{SV} = (\mathbf{Q}_Y \mathbf{U}_B) \boldsymbol{\Sigma} \widehat{\mathbf{V}}^\top$ . The approximation of the Gram product is now straightforward

$$\mathbf{H} \approx \widehat{\mathbf{H}}_{SV} \equiv \mathbf{A}_{SV}^\top \mathbf{A}_{SV} = \widehat{\mathbf{V}} \widehat{\boldsymbol{\Lambda}} \widehat{\mathbf{V}}^\top,$$

where  $\widehat{\boldsymbol{\Lambda}} = \boldsymbol{\Sigma}^2$ .

Because the oblique projector introduces some numerical issues a standard approach is to use additional oversampling. In [42, Theorem 4.3], one recommendation is to use  $\ell_1 = 2r + 1$  and  $\ell_2 = 2\ell_1 + 1$ , where  $r$  is the target rank. In our numerical experiments, we take  $\ell_1$  to be equal to  $\ell$  as in the previously discussed RandSVD and Nyström methods to compare the methods on an even footing. Note that this approach requires more ADJ solves (and TLM solves if  $\ell_1 > \ell$ ) than the previously discussed methods, but the key point here is that these ADJ and TLM solves can each be performed in parallel simultaneously, thus exposing an additional layer of parallelism.

---

**Algorithm 3** SingleView GN Hessian Approximation

---

**Require:** Operator:  $\mathbf{A} \in \mathbb{R}^{m \times n}$ , sketch parameters:  $\ell_1, \ell_2$  (with  $\ell_2 \geq \ell_1$ ).

- 1: Draw Gaussian random matrices  $\boldsymbol{\Omega} \in \mathbb{R}^{n \times \ell_1}$ ,  $\boldsymbol{\Psi} \in \mathbb{R}^{m \times \ell_2}$
  - 2: Compute sketches  $\mathbf{Y} = \mathbf{A} \boldsymbol{\Omega}$  and  $\mathbf{Z} = \mathbf{A}^\top \boldsymbol{\Psi}$  {Compute, if possible, in parallel}
  - 3: Compute thin-QR factorization of  $\mathbf{Y} = \mathbf{Q}_Y \mathbf{R}_Y$
  - 4: Compute thin-QR factorization of  $\mathbf{M} = \boldsymbol{\Psi}^\top \mathbf{Q}_Y = \mathbf{Q}_M \mathbf{R}_M$
  - 5: Compute  $\mathbf{W} = \mathbf{R}_M^\dagger (\mathbf{Z} \mathbf{Q}_M)^\top$  and its thin-SVD  $\mathbf{W} = \widehat{\mathbf{U}} \widehat{\boldsymbol{\Sigma}} \widehat{\mathbf{V}}^\top$
  - 6: **return** Matrices  $\widehat{\mathbf{V}}, \widehat{\boldsymbol{\Lambda}} = \boldsymbol{\Sigma}^2$  that defines the approximation  $\widehat{\mathbf{H}}_{SV} = \widehat{\mathbf{V}} \widehat{\boldsymbol{\Lambda}} \widehat{\mathbf{V}}^\top$
- 

### 3.1.2. Adaptive sketching

In many applications, the spectrum of  $\mathbf{H}$ , can vary across the iterates ( $k$ ), and the choice of a fixed  $\ell$  may be inappropriate. To this end, we design a methodology to adaptively choose  $\ell$  based on the condition number of the GN Hessian in eq. (10). We use the following quantity  $\kappa_{sk}$  as an estimate for the accuracy of  $\mathcal{H}$

$$\kappa_{sk} = \frac{\mathbf{v}^\top \widehat{\mathcal{H}}^{-1} \mathcal{H} \widehat{\mathcal{H}}^{-1} \mathbf{v}}{\mathbf{v}^\top \widehat{\mathcal{H}}^{-1} \mathbf{v}}, \quad (15)$$

where  $\mathbf{v} \sim \mathcal{N}(\mathbf{0}, \mathbf{I})$  is a normal random test vector. Note that for any nonzero vector  $\mathbf{v}$  and for any approximation satisfying  $\mathcal{H} \succeq \widehat{\mathcal{H}}$ , we have the inequality

$$\|\widehat{\mathcal{H}}^{-1/2} \mathcal{H} \widehat{\mathcal{H}}^{-1/2}\|_2 \geq \frac{\mathbf{v}^\top \widehat{\mathcal{H}}^{-1} \mathcal{H} \widehat{\mathcal{H}}^{-1} \mathbf{v}}{\mathbf{v}^\top \widehat{\mathcal{H}}^{-1} \mathbf{v}} = \kappa_{sk} \geq 1, \quad (16)$$

which follows from the optimality of the Rayleigh quotient and the assumption  $\mathcal{H} \succeq \widehat{\mathcal{H}}$ . As will be shown in Section 4, both the RandSVD and Nyström approximations satisfy  $\mathcal{H} \succeq \widehat{\mathcal{H}}$ .

The idea behind the adaptive sketching approach is (i) to construct a sketch  $\widehat{\mathcal{H}}$  with an initial choice of  $\ell$ ; (ii) while  $\kappa_{sk}^{-1} < \epsilon_{sk}$ , recompute a new sketch with incremented  $\ell$ ; Here  $\epsilon_{sk}$  is

some chosen threshold in  $(0, 1]$ . While all three methods can be made adaptive, we specifically focus on RandSVD only, due to the low computational overhead to make adaptive. The details of the algorithm are provided in Algorithm 4.

---

**Algorithm 4** Adaptive RandSVD GN Hessian Approximation

---

**Require:** Operator:  $\mathbf{A} \in \mathbb{R}^{m \times n}$ , sketch parameters:  $\ell, \hat{\ell}, \epsilon_{\text{sk}}$ .

- 1: Draw Gaussian random matrix  $\mathbf{\Omega} \in \mathbb{R}^{n \times \ell}$ .
  - 2: Compute forward pass  $\mathbf{Y} = \mathbf{A}\mathbf{\Omega}$ . {Compute, if possible, in parallel}
  - 3: Compute thin -QR factorization  $\mathbf{Y} = \mathbf{Q}\mathbf{R}$ .
  - 4: Compute  $\mathbf{W}^\top = \mathbf{A}^\top \mathbf{Q}$ . {Compute, if possible, in parallel}
  - 5: **while**  $\kappa_{sk}^{-1} < \epsilon_{\text{sk}}$  **do**
  - 6:   Draw Gaussian random matrix  $\hat{\mathbf{\Omega}} \in \mathbb{R}^{n \times \hat{\ell}}$ .
  - 7:   Compute forward pass  $\mathbf{Y} = \mathbf{A}\hat{\mathbf{\Omega}}$ . {Compute, if possible, in parallel}
  - 8:   Orthogonalize  $\mathbf{Y} = \mathbf{Y} - \mathbf{Q}(\mathbf{Q}^\top \mathbf{Y})$ . {Additional Gram-Schmidt orthogonalization steps, if necessary.}
  - 9:   Compute thin-QR factorization  $\mathbf{Y} = \hat{\mathbf{Q}}\mathbf{R}$ .
  - 10:   Compute  $\hat{\mathbf{W}}^\top = \mathbf{A}^\top \hat{\mathbf{Q}}$ . {Compute, if possible, in Parallel}
  - 11:   Update  $\ell \leftarrow \ell + \hat{\ell}$ ,  $\mathbf{W} \leftarrow \begin{bmatrix} \mathbf{W}^\top & \hat{\mathbf{W}}^\top \end{bmatrix}^\top$ ,  $\mathbf{Q} \leftarrow \begin{bmatrix} \mathbf{Q} & \hat{\mathbf{Q}} \end{bmatrix}$
  - 12: **end while**
  - 13: Compute thin-SVD  $\mathbf{W} = \hat{\mathbf{U}}\hat{\mathbf{\Sigma}}\hat{\mathbf{V}}^\top$ ,  $\hat{\mathbf{\Lambda}} = \hat{\mathbf{\Sigma}}^2$ .
  - 14: **return** Matrices  $\hat{\mathbf{V}}, \hat{\mathbf{\Lambda}}$  that defines the approximation  $\hat{\mathbf{H}} = \hat{\mathbf{V}}\hat{\mathbf{\Lambda}}\hat{\mathbf{V}}^\top$ .
- 

### 3.1.3. Comparison of computational costs

We now compare the proposed approaches in terms of the computational costs and scope for parallelism. To compare the approaches on the same footing, assume that each TLM and ADJ run costs the same. In Table 1, we summarize the computational costs, and in reporting the costs we assume that  $\ell, \ell_1, \ell_2 = \mathcal{O}(r)$ . As can be seen, in a serial implementation, the computational costs of RandSVD and Nyström are very similar, with RandSVD having a slightly lower cost when  $m \ll n$ . Furthermore, SingleView is the most expensive of the three algorithms, although it is more parallelizable.

Method	TLM	ADJ	Prior	Additional (flops)	PPE (%)
RandSVD	$\ell$	$\ell$	$2\ell$	$\mathcal{O}(r^3 + r^2(m + n))$	50
Nyström	$\ell$	$\ell$	$2\ell$	$\mathcal{O}(r^3 + r^2n)$	50
SingleView	$\ell_1$	$\ell_2$	$\ell_1 + \ell_2$	$\mathcal{O}(r^3 + r^2(m + n))$	100

Table 1: Comparison of computational costs for a single GN approximation. PPE refers to peak parallel efficiency.

Assume that we have a sufficiently large number of processors available. We define **peak parallel efficiency** (or PPE) as the percentage of the maximum number of PDE solves that can be run in parallel at any given time to the total number of PDE solves that need to be run. Then, for RandSVD, we can perform  $\ell$  TLM solves in parallel (to compute  $\mathbf{Y} = \mathbf{A}\mathbf{\Omega}$ ) followed  $\ell$  ADJ solves in parallel (to compute  $\mathbf{Z} = \mathbf{A}^\top \mathbf{Q}$ ). This gives this method the PPE of 50%. The Nyström approach similarly has a PPE of 50%. However, in the SingleView approach, both the TLM and ADJ solves can be done simultaneously in parallel, so it has a PPE of 100%.

There are other forms of parallelism in solving PDEs [18, 29] such as parallelism in the spatial and temporal dimensions that are not explored here but may have further increase the gains from parallelism from our approach.

### 3.2. Combining sketching with optimization

In this section, we discuss the usage of the computed sketch for the GN optimization routine.

#### 3.2.1. SketchSolv

In this approach, we solve for the GN step approximately using the low-rank approximation for  $\mathbf{H}$  as

$$\widehat{\delta\mathbf{x}} = -\widehat{\mathcal{H}}^{-1}\mathbf{g} = -\mathbf{\Gamma}^{1/2}\left(\mathbf{I} - \widehat{\mathbf{V}}(\widehat{\mathbf{\Lambda}}^{-1} + \mathbf{I})^{-1}\widehat{\mathbf{V}}^\top\right)\mathbf{\Gamma}^{1/2}\mathbf{g}. \quad (17)$$

Similar to inexact GN, the optimization proceeds by using an inexact GN step that can be computed more efficiently than the exact GN step. It may be possible to combine the convergence analysis of inexact GN with the guarantees using the SketchSolv approach, but we did not pursue this analysis.

#### 3.2.2. SketchPrec

In this approach, we use the GN Hessian approximation  $\widehat{\mathcal{H}}^{-1}$  (either fixed or adaptive rank) as a preconditioner to solve eq. (10) using PCG. In the most basic version, the sketch  $\widehat{\mathcal{H}}$  is recomputed at every  $(k)^{th}$  GN iteration. While this may appear computationally expensive, it has two benefits: the costs involving TLM/ADJ solves can be applied in parallel, and as the experiments show, the total number of TLM/ADJ solves is also reduced (even after including the expense of constructing the preconditioner). Therefore, the preconditioner has benefits both in the serial and distributed settings.

An alternative approach that we pursue here is to reuse the preconditioners across multiple GN iterations. That is, to solve the system (10), we precondition with a previous sketch (e.g.,  $k - i$ th GN iteration,  $(\widehat{\mathcal{H}}^{(k-i)})^{-1}$ ), where  $0 \leq i < k$ . To determine the effectiveness of the preconditioner, we use the following heuristic, based on eq. (15). Define the quantity

$$\kappa_{re} := \frac{\mathbf{v}^\top \left(\widehat{\mathcal{H}}^{(k-i)}\right)^{-1} \mathcal{H} \left(\widehat{\mathcal{H}}^{(k-i)}\right)^{-1} \mathbf{v}}{\mathbf{v}^\top \left(\widehat{\mathcal{H}}^{(k-i)}\right)^{-1} \mathbf{v}}, \quad (18)$$

where, as before,  $\mathbf{v} \sim \mathcal{N}(\mathbf{0}, \mathbf{I})$ . Note that the bound  $\kappa_{re} \geq 1$  need not hold, but  $\kappa_{re}$  is still a lower bound to the matrix

$$\left(\widehat{\mathcal{H}}^{(k-i)}\right)^{-1/2} \mathcal{H} \left(\widehat{\mathcal{H}}^{(k-i)}\right)^{-1/2}. \quad (19)$$

The heuristic we propose is to reuse the sketch if  $\kappa_{re}^{-1} < \epsilon_{re}$ , where  $\epsilon_{re}$  is a user-specified tolerance on which we comment briefly below. At each GN iteration, we use the above heuristic to determine whether to reuse or update the preconditioner. If the preconditioner is updated, then we use the adaptive approach in Algorithm 4. Therefore, adaptivity is used in two ways: to determine when to update the sketch and the sketch size.

We comment on the choice of the parameter  $\epsilon_{re}$  and its relation to  $\epsilon_{sk}$ . First, we choose  $\epsilon_{sk} \geq \epsilon_{re}$ , meaning that we use a more stringent criterion for computing a sketched preconditioner than we use for deciding to reuse a preconditioner. The choice of a high  $\epsilon_{re}$  (close to 1), requires

more resketching, which gives better preconditioners at the cost of a higher flop count, whereas a moderate  $\epsilon_{\text{re}}$  (0.1–0.7) would allow for flexible reuse of a previous preconditioner, at the cost of being slightly sub-optimal, and a low  $\epsilon_{\text{re}}$  ( $< 0.1$ ) could result in the reuse of a poor preconditioner. In our experiments, we observed that for a fixed  $\epsilon_{\text{re}}$ , a higher  $\epsilon_{\text{sk}}$  (around 0.4–0.9) results in fewer resketches. This is because a “more accurate” (based on  $\epsilon_{\text{re}}$ ) preconditioner from a previous GN iteration is still adequate as a preconditioner (based on  $\epsilon_{\text{re}}$ ) in the current GN iteration. We also observed the converse, where a low  $\epsilon_{\text{sk}}$  (approximately  $< 0.2$ ), resulted in more recomputations of the preconditioner across Gauss-Newton iterations as the “less accurate” preconditioner from a previous GN iteration is typically inadequate for the current GN iteration. Ultimately, the choice of  $\epsilon_{\text{sk}}$  and  $\epsilon_{\text{re}}$  is problem and resource-specific.

In SketchPrec, the use of randomization accelerates the overall convergence of GN. This is a primary advantage of the sketch and precondition paradigm [24, Section 10.5].

### 3.3. Other applications of the preconditioner

After the MAP point has been determined by solving the nonlinear optimization problem, it is common to perform uncertainty quantification (UQ) by linearizing the forward operator at the MAP point. This can be viewed as a Gaussian approximation to the posterior distribution. Uncertainty quantification involving the approximate posterior distribution can come in two forms: samples from the distribution, and the posterior variance estimates. Both of these tasks can be accomplished by using the preconditioned Lanczos approach; see [30]. Note that in practice, several samples from the (approximate) posterior are desired, or to compute the posterior variance, several applications of the posterior covariance (inverse of the Hessian) are necessary. If a preconditioner is constructed at the MAP point, it can be used to accelerate the Lanczos approach for both tasks; furthermore, the cost of constructing a preconditioner is well justified since the same preconditioner can be used across many posterior sample computations.

## 4. Analysis of the sketching methods

In this section, we provide error analysis for the previously proposed sketching methods. Our analysis applies only to a single step of the appropriate optimization algorithm and focuses on three different quantities:

1. Error in the GN step: When the randomized sketch is used in SketchSolv, we bound the error in the GN step at the current iterate.
2. Condition number: When the randomized sketch is used in SketchPrec, we bound the 2-norm condition number of the preconditioned operator. When this is used as a preconditioner for CG, this result can be combined with the analysis for the reduction in the error in the  $\|\cdot\|_{\mathcal{H}}$ -norm with iterations [40, Theorem 38.5].
3. Error in the inverse: When the randomized sketch is used in SketchInit, we bound the relative error in the GN Hessian inverse.

### 4.1. Setup for the analysis

We first establish some notation. Recall that we have defined  $\mathbf{A} = \mathbf{G}\mathbf{\Gamma}^{1/2}$  and we assume it has the compact SVD  $\mathbf{A} = \mathbf{U}\mathbf{\Sigma}\mathbf{V}^\top$ . We assume that the number of measurements  $m \leq n$ . The eigenvalues of the data-misfit Hessian  $\mathbf{H}$  are

$$\lambda_1 = \sigma_1^2, \dots, \lambda_m = \sigma_m^2, \lambda_{m+1} = \dots = \lambda_n = 0. \quad (20)$$

Partition the SVD of  $\mathbf{A}$  as

$$\mathbf{A} = [\mathbf{U}_1 \quad \mathbf{U}_2] \begin{bmatrix} \boldsymbol{\Sigma}_1 & \\ & \boldsymbol{\Sigma}_2 \end{bmatrix} \begin{bmatrix} \mathbf{V}_1^\top \\ \mathbf{V}_2^\top \end{bmatrix}, \quad (21)$$

where  $\boldsymbol{\Sigma}_1 \in \mathbb{R}^{r \times r}$ ,  $\mathbf{U}_1 \in \mathbb{R}^{m \times r}$ , and  $\mathbf{V}_1 \in \mathbb{R}^{n \times r}$ . Here  $r \leq m$  is the target rank.

We will need the norm  $\|\mathbf{x}\|_{\mathbf{M}} = \|\mathbf{M}^{1/2}\mathbf{x}\|_2$  which is a valid vector norm for any symmetric positive definite matrix  $\mathbf{M}$ . When  $\mathbf{M}$  is symmetric positive semidefinite  $\|\mathbf{M}^{1/2}\|_2 = \|\mathbf{M}\|_2^{1/2}$ . This satisfies the inequality

$$\frac{\|\mathbf{x}\|_2}{\sqrt{\|\mathbf{M}^{-1}\|_2}} \leq \|\mathbf{x}\|_{\mathbf{M}} \leq \sqrt{\|\mathbf{M}\|_2} \|\mathbf{x}\|_2. \quad (22)$$

For an invertible matrix  $\mathbf{M}$ , we define the 2-norm condition number for inversion as  $\kappa_2(\mathbf{M}) = \|\mathbf{M}\|_2 \|\mathbf{M}^{-1}\|_2$ .

We say two symmetric matrices  $\mathbf{C}, \mathbf{D} \in \mathbb{R}^{n \times n}$  satisfy  $\mathbf{C} \preceq \mathbf{D}$  (equivalently,  $\mathbf{D} \succeq \mathbf{C}$ ) if  $\mathbf{D} - \mathbf{C}$  is positive semidefinite. For any  $\mathbf{X} \in \mathbb{R}^{m \times n}$ , we have  $\mathbf{X}\mathbf{C}\mathbf{X}^\top \preceq \mathbf{X}\mathbf{D}\mathbf{X}^\top$  and for any symmetric  $\mathbf{M} \in \mathbb{R}^{n \times n}$ ,  $\mathbf{C} + \mathbf{M} \preceq \mathbf{D} + \mathbf{M}$ . If additionally both  $\mathbf{C}, \mathbf{D}$  are positive definite, then  $\mathbf{D}^{-1} \preceq \mathbf{C}^{-1}$ .

#### 4.2. Summary of main results

In this section, we assume that  $\lambda_{r+1} \neq 0$ . Let us define

$$\text{id}_r \equiv \frac{\sum_{j>r} \lambda_j}{\lambda_{r+1}}$$

as the *intrinsic dimension* of the tail of the eigenvalues. This is also the stable rank of the matrix  $\boldsymbol{\Sigma}_2$ . This quantity is important in our analysis.

In many applications, the eigenvalues of the operator  $\mathbf{H}$  decay rapidly, so that the intrinsic dimension  $\text{id}_r$  is often bound independent of the dimensions of the operator. In analogy with the decay of the singular values of the Fredholm integral equation in deterministic inverse problems [21, Section 1.2.2], we consider two cases:

1. **Moderately ill-posed:** We say that the problem is moderately ill-posed if  $\lambda_j = C_m j^{-\alpha}$  where  $C_m$  is a constant,  $\alpha > 1$ . Then the intrinsic dimension is bounded by

$$\text{id}_r \leq \frac{1}{\lambda_{r+1}} \sum_{j>r}^{\infty} \lambda_j = \zeta(\alpha),$$

where  $\zeta$  is the Riemann zeta function. If  $\alpha \leq 1$ , the problem is said to be mildly ill-posed, which we do not consider, since the tail is not summable.

2. **Severely ill-posed:** We say that the problem is severely ill-posed if  $\lambda_j = C_s \exp(-\alpha j)$  where  $\alpha > 0$  and  $C_s$  is a constant.

$$\text{id}_r \leq \frac{1}{\lambda_{r+1}} \sum_{j>r}^{\infty} \lambda_j = \frac{1}{(1 - e^{-\alpha})}.$$

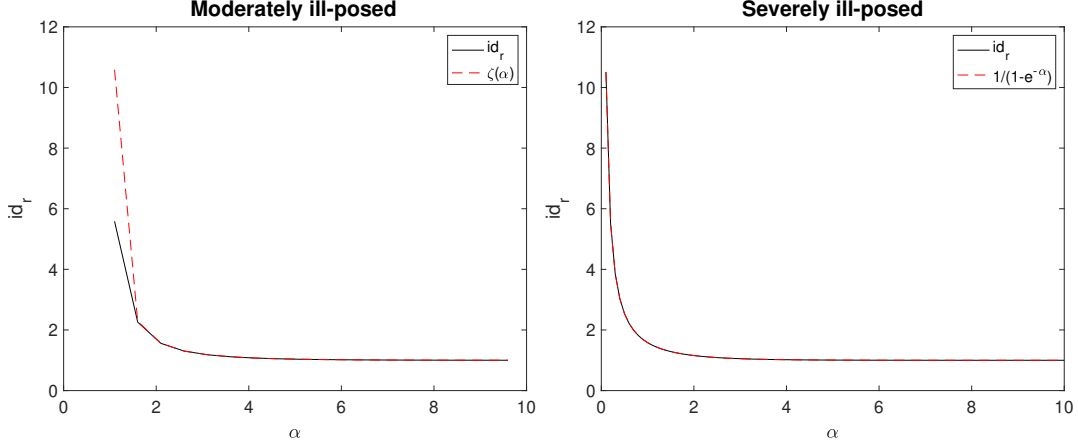


Figure 1: Plot of intrinsic dimension and the bounds for (left) moderately and (right) severely ill-posed cases.

The bounds that we present below all involve the intrinsic dimension  $\text{id}_r$  and do not show explicit dependence on the dimension of the matrices. To illustrate the intrinsic dimension consider the case  $n - r = 1024$ ; we plot the intrinsic dimension as a function of  $\alpha$  for the moderately and severely ill-posed cases in Figure 1. As can be seen, the intrinsic dimension decreases with the decay parameter  $\alpha$  in both cases. Furthermore, this dimension is much smaller than the number of grid points  $n$ .

We first derive bounds for the RandSVD algorithm.

**Theorem 1** (RandSVD). *Let  $\mathbf{\Omega} \in \mathbb{R}^{n \times \ell}$  be a standard Gaussian random matrix which is an input to Algorithm 1, where  $\ell = r + p$ ,  $r$  is the target rank and  $p \geq 2$  is an oversampling parameter. Consider the output of Algorithm 1,  $\widehat{\mathbf{H}}$ , and define  $\widehat{\mathcal{H}} = \mathbf{\Gamma}^{-1/2}(\mathbf{I} + \widehat{\mathbf{H}})\mathbf{\Gamma}^{-1/2}$ . Let*

$$\Psi_{\mathbf{H}}(r, p) \equiv \lambda_{r+1} + \frac{r}{p-1} \sum_{j>r} \lambda_j = \left(1 + \frac{r}{p-1} \text{id}_r\right) \lambda_{r+1}.$$

We have the following bounds:

1. The error in the solution (defined as eq. (17)) satisfies

$$\mathbb{E} \left[ \frac{\|\delta \mathbf{x} - \delta \widehat{\mathbf{x}}\|_{\mathbf{\Gamma}^{-1}}}{\|\delta \mathbf{x}\|_{\mathbf{\Gamma}^{-1}}} \right] \leq \Psi_{\mathbf{H}}(r, p).$$

2. The condition number of the preconditioned operator satisfies

$$\mathbb{E} \left[ \kappa_2(\widehat{\mathcal{H}}^{-1/2} \mathcal{H} \widehat{\mathcal{H}}^{-1/2}) \right] \leq 1 + \sqrt{\kappa_2(\mathbf{\Gamma})} \Psi_{\mathbf{H}}(r, p).$$

3. The error in the inverse satisfies

$$\mathbb{E} \left[ \frac{\|\mathcal{H}^{-1} - \widehat{\mathcal{H}}^{-1}\|_2}{\|\mathcal{H}^{-1}\|_2} \right] \leq \sqrt{\kappa_2(\mathbf{\Gamma})} \Psi_{\mathbf{H}}(r, p).$$

*Proof.* See Section 4.4. □

*Number of samples.* We now discuss how to select the number of samples  $\ell$ . Assume that  $r_\epsilon$  is the largest index such that  $\lambda_j \leq \epsilon$  for all  $j > r_\epsilon$ , and where  $\epsilon$  is a user-specified threshold. If we take  $\ell = \lceil \frac{6}{5}r_\epsilon + 1 \rceil$ , then

$$\Psi_{\mathbf{H}}(r, p) \leq (1 + 5\text{id}_{r_\epsilon}) \epsilon.$$

We can then readily bound the appropriate quantities in Theorem 1. For example

$$\mathbb{E} \left[ \kappa_2(\widehat{\mathcal{H}}^{-1/2} \mathcal{H} \widehat{\mathcal{H}}^{-1/2}) \right] \leq 1 + \sqrt{\kappa_2(\mathbf{\Gamma})} (1 + 5\text{id}_{r_*}) \epsilon.$$

With this simplified representation, we can now interpret the results of Theorem 1. The condition number of the preconditioned system is close to 1, provided that the condition number of the prior covariance is small and the eigenvalues of  $\mathbf{H}$  are decaying rapidly (either moderately or severely ill-posed). Similarly, the error in the GN step is small in the  $\|\cdot\|_{\mathbf{\Gamma}^{-1}}$  norm and the error in the GN Hessian are small, under the same conditions.

We now provide analysis for the Nyström sketch.

**Theorem 2** (Nyström). *Let  $\mathbf{\Omega} \in \mathbb{R}^{n \times \ell}$  be a standard Gaussian random matrix which is an input to Algorithm 2, where  $\ell = r + p$ ,  $r$  is the target rank and  $p \geq 2$  is an oversampling parameter. Consider the output of Algorithm 2,  $\widehat{\mathbf{H}}$ , and define  $\widehat{\mathcal{H}} = \mathbf{\Gamma}^{-1/2}(\mathbf{I} + \widehat{\mathbf{H}})\mathbf{\Gamma}^{-1/2}$ . Then, with  $\Psi_{\mathbf{H}}(r, p)$  as defined in Theorem 1*

1. *The error in the solution satisfies*

$$\mathbb{E} \left[ \frac{\|\delta \mathbf{x} - \delta \widehat{\mathbf{x}}\|_{\mathbf{\Gamma}^{-1}}}{\|\delta \mathbf{x}\|_{\mathbf{\Gamma}^{-1}}} \right] \leq \Psi_{\mathbf{H}}(r, p).$$

2. *The condition number of the preconditioned operator satisfies*

$$\mathbb{E} \left[ \kappa_2(\widehat{\mathcal{H}}^{-1/2} \mathcal{H} \widehat{\mathcal{H}}^{-1/2}) \right] \leq 1 + \sqrt{\kappa_2(\mathbf{\Gamma})} \Psi_{\mathbf{H}}(r, p).$$

3. *The error in the inverse satisfies*

$$\mathbb{E} \left[ \frac{\|\mathcal{H}^{-1} - \widehat{\mathcal{H}}^{-1}\|_2}{\|\mathcal{H}^{-1}\|_2} \right] \leq \sqrt{\kappa_2(\mathbf{\Gamma})} \Psi_{\mathbf{H}}(r, p).$$

*Proof.* See Section 4.4. □

Surprisingly, both RandSVD and Nyström approximations give identical upper bounds in expectation. Both methods are also comparable in computational cost. The interpretation of Nyström is, therefore, similar to RandSVD. Finally, we turn to the analysis of the SingleView sketch.

**Theorem 3** (SingleView). *Suppose  $\mathbf{\Omega} \in \mathbb{R}^{n \times \ell_1}$  and  $\mathbf{\Psi} \in \mathbb{R}^{m \times \ell_2}$  (standard Gaussian random matrices) are inputs to Algorithm 3, where  $\ell_1 = 2r + 1$ ,  $\ell_2 = 2\ell_1 + 1 = 4r + 3$  and  $r$  is the target rank. Consider the output of Algorithm 3,  $\widehat{\mathbf{H}}$ , and define  $\widehat{\mathcal{H}} = \mathbf{\Gamma}^{-1/2}(\mathbf{I} + \widehat{\mathbf{H}})\mathbf{\Gamma}^{-1/2}$ . Let*

$$\Theta_{\mathbf{H}}(r, p) \equiv 3 \left( \sum_{j>r} \lambda_1 \lambda_j \right)^{1/2} + \frac{9}{4} \left( \sum_{j>r} \lambda_j \right) = \left( 3 \left( \frac{\lambda_1}{\lambda_{r+1}} \right)^{1/2} \text{id}_r^{1/2} + \frac{9}{4} \text{id}_r \right) \lambda_{r+1}.$$

Then

1. The error in the solution satisfies

$$\mathbb{E} \left[ \frac{\|\delta\mathbf{x} - \delta\hat{\mathbf{x}}\|_{\Gamma^{-1}}}{\|\delta\mathbf{x}\|_{\Gamma^{-1}}} \right] \leq \Theta_{\mathbf{H}}(r, p).$$

2. The condition number of the preconditioned operator satisfies

$$\mathbb{E} \left[ \sqrt{\kappa_2(\hat{\mathcal{H}}^{-1/2} \mathcal{H} \hat{\mathcal{H}}^{-1/2})} \right] \leq 1 + \sqrt{\kappa_2(\Gamma)} \Theta_{\mathbf{H}}(r, p).$$

3. The error in the inverse satisfies

$$\mathbb{E} \left[ \frac{\|\mathcal{H}^{-1} - \hat{\mathcal{H}}^{-1}\|_2}{\|\mathcal{H}^{-1}\|_2} \right] \leq \sqrt{\kappa_2(\Gamma)} \Theta_{\mathbf{H}}(r, p).$$

*Proof.* See Section 4.4. □

The results of SingleView are considerably weaker than RandSVD and Nyström. We see the appearance of  $\lambda_1$  in the bounds, which can be large. Furthermore, we are only able to bound the expected value of the square root of the condition number. We explain these reasons in Section 4.4.

#### 4.3. Structural analysis

In the analysis below, the error  $\mathbf{E} = \mathbf{H} - \hat{\mathbf{H}}$  plays an important role. We consider two different cases:  $\mathbf{E} \succeq \mathbf{0}$ , and otherwise. This distinction is important because, with the stronger assumption  $\mathbf{E} \succeq \mathbf{0}$ , we can obtain tighter bounds in some cases. This assumption is satisfied for two of the methods (RandSVD and Nyström) as we will show. We call this analysis *structural* because it does not take into account the randomness of the inputs. It applies to any approximation  $\mathbf{H} \approx \hat{\mathbf{H}}$ , that need not be a randomized or even a low-rank approximation.

Our first result quantifies the error in the solution of the linear system.

**Theorem 4** (Error in solve). *Let  $\mathbf{E} = \mathbf{H} - \hat{\mathbf{H}}$  denote the error in the low-rank approximation. The relative error in the linear system satisfies*

$$\frac{\|\delta\mathbf{x} - \delta\hat{\mathbf{x}}\|_{\Gamma^{-1}}}{\|\delta\mathbf{x}\|_{\Gamma^{-1}}} \leq \|\mathbf{E}\|_2.$$

This result has similarities to [15, Proposition 3.1], but applies to a more general covariance matrix. The interpretation of this bound is that the error is small if  $\|\mathbf{E}\|_2$  is small. We were not able to obtain a tighter bound if, additionally,  $\mathbf{E} \succeq \mathbf{0}$  holds. The analysis bounds the error in the  $\|\cdot\|_{\Gamma^{-1}}$  norm; if, however, the error is desired in the 2-norm, we can equivalently write

$$\frac{\|\delta\mathbf{x} - \delta\hat{\mathbf{x}}\|_2}{\|\delta\mathbf{x}\|_2} \leq \sqrt{\kappa_2(\Gamma)} \frac{\|\delta\mathbf{x} - \delta\hat{\mathbf{x}}\|_{\Gamma^{-1}}}{\|\delta\mathbf{x}\|_{\Gamma^{-1}}} \leq \sqrt{\kappa_2(\Gamma)} \|\mathbf{E}\|_2.$$

*Proof of Theorem 4.* Observe that

$$\mathcal{H} = \Gamma^{-1/2}(\hat{\mathcal{H}} + \mathbf{E})\Gamma^{-1/2} = \hat{\mathcal{H}} + \Gamma^{-1/2}\mathbf{E}\Gamma^{-1/2}.$$

From  $\widehat{\mathcal{H}}\delta\widehat{\mathbf{x}} = -\mathbf{g} = \mathcal{H}\delta\mathbf{x}$ , we can write

$$\widehat{\mathcal{H}}(\delta\widehat{\mathbf{x}} - \delta\mathbf{x}) = (\mathcal{H} - \widehat{\mathcal{H}})\delta\mathbf{x} = \mathbf{\Gamma}^{-1/2}\mathbf{E}\mathbf{\Gamma}^{-1/2}\delta\mathbf{x}.$$

On the left hand side, we expand  $\widehat{\mathcal{H}}$ , we get

$$\mathbf{\Gamma}^{-1/2}(\mathbf{I} + \widehat{\mathbf{H}})\mathbf{\Gamma}^{-1/2}(\delta\widehat{\mathbf{x}} - \delta\mathbf{x}) = \mathbf{\Gamma}^{-1/2}\mathbf{E}\mathbf{\Gamma}^{-1/2}\delta\mathbf{x},$$

which simplifies to  $\mathbf{\Gamma}^{-1/2}(\delta\widehat{\mathbf{x}} - \delta\mathbf{x}) = (\mathbf{I} + \widehat{\mathbf{H}})^{-1}\mathbf{E}\mathbf{\Gamma}^{-1/2}\delta\mathbf{x}$ . Using submultiplicativity

$$\|(\delta\widehat{\mathbf{x}} - \delta\mathbf{x})\|_{\mathbf{\Gamma}^{-1}} \leq \|(\mathbf{I} + \widehat{\mathbf{H}})^{-1}\|_2 \|\mathbf{E}\|_2 \|\delta\mathbf{x}\|_{\mathbf{\Gamma}^{-1}}.$$

The proof is complete by noting that the singular values of  $(\mathbf{I} + \widehat{\mathbf{H}})$  are at least 1.  $\square$

Next, we bound the error in the inverse since the same technique applies to the bound on the condition number.

**Theorem 5** (Error in inverse). *Let  $\mathbf{E} = \mathbf{H} - \widehat{\mathbf{H}}$  denote the error in the low-rank approximation. Then, the relative error in the inverse satisfies*

$$\frac{\|\mathcal{H}^{-1} - \widehat{\mathcal{H}}^{-1}\|_2}{\|\mathcal{H}^{-1}\|_2} \leq \sqrt{\kappa_2(\mathbf{\Gamma})} \|\mathbf{E}\|_2.$$

The interpretation of the theorem is similar to that of Theorem 4.

*Proof of Theorem 5.* We first write  $(\mathcal{H}^{-1} - \widehat{\mathcal{H}}^{-1}) = \mathcal{H}^{-1}(\mathbf{I} - \mathcal{H}\widehat{\mathcal{H}}^{-1})$ . Applying submultiplicativity,

$$\|\mathcal{H}^{-1} - \widehat{\mathcal{H}}^{-1}\|_2 \leq \|\mathcal{H}^{-1}\|_2 \|\mathbf{I} - \mathcal{H}\widehat{\mathcal{H}}^{-1}\|_2.$$

We rewrite  $\mathbf{I} - \mathcal{H}\widehat{\mathcal{H}}^{-1} = -(\mathbf{H} - \widehat{\mathbf{H}})(\mathbf{I} + \widehat{\mathbf{H}})^{-1}\mathbf{\Gamma}^{1/2} = -\mathbf{\Gamma}^{-1/2}\mathbf{E}(\mathbf{I} + \widehat{\mathbf{H}})^{-1}\mathbf{\Gamma}^{1/2}$ . The rest of the proof follows by applying submultiplicativity and noting  $\|(\mathbf{I} + \widehat{\mathbf{H}})^{-1}\|_2 \leq 1$ .  $\square$

We now analyze the condition number of the preconditioned matrix.

**Theorem 6** (Condition number bound). *Let  $\mathbf{E} = \mathbf{H} - \widehat{\mathbf{H}}$ . Then*

$$\kappa_2(\widehat{\mathcal{H}}^{-1/2}\mathcal{H}\widehat{\mathcal{H}}^{-1/2}) \leq \left(1 + \sqrt{\kappa_2(\mathbf{\Gamma})}\|\mathbf{E}\|_2\right)^2.$$

*Suppose, additionally, that  $\mathbf{E} \succeq \mathbf{0}$ , then*

$$\kappa_2(\widehat{\mathcal{H}}^{-1/2}\mathcal{H}\widehat{\mathcal{H}}^{-1/2}) \leq 1 + \sqrt{\kappa_2(\mathbf{\Gamma})}\|\mathbf{E}\|_2.$$

It is clear from the theorem that the bound is tighter when  $\mathbf{E} \succeq \mathbf{0}$ . The interpretation of this theorem is similar to the others in this section.

*Proof.* By definition, the condition number is

$$\kappa_2(\widehat{\mathcal{H}}^{-1/2}\mathcal{H}\widehat{\mathcal{H}}^{-1/2}) = \underbrace{\|\widehat{\mathcal{H}}^{-1/2}\mathcal{H}\widehat{\mathcal{H}}^{-1/2}\|_2}_{\alpha} \underbrace{\|\widehat{\mathcal{H}}^{1/2}\mathcal{H}^{-1}\widehat{\mathcal{H}}^{1/2}\|_2}_{\beta}.$$

We bound the two terms separately.

To bound  $\alpha$ , we write  $\mathcal{H} = \mathcal{H} - \widehat{\mathcal{H}} + \widehat{\mathcal{H}}$ , so that

$$\widehat{\mathcal{H}}^{-1/2} \mathcal{H} \widehat{\mathcal{H}}^{-1/2} = \mathbf{I} + \widehat{\mathcal{H}}^{-1/2} (\mathcal{H} - \widehat{\mathcal{H}}) \widehat{\mathcal{H}}^{-1/2}.$$

Therefore, using the triangle inequality  $\alpha \leq 1 + \|\widehat{\mathcal{H}}^{-1/2} (\mathcal{H} - \widehat{\mathcal{H}}) \widehat{\mathcal{H}}^{-1/2}\|_2$ . Using [3, Proposition IX.1.1],

$$\|\widehat{\mathcal{H}}^{-1/2} (\mathcal{H} - \widehat{\mathcal{H}}) \widehat{\mathcal{H}}^{-1/2}\|_2 \leq \|(\mathcal{H} - \widehat{\mathcal{H}}) \widehat{\mathcal{H}}^{-1}\|_2.$$

The term inside the norm can be simplified as

$$(\mathcal{H} - \widehat{\mathcal{H}}) \widehat{\mathcal{H}}^{-1} = \mathbf{\Gamma}^{-1/2} (\mathbf{H} - \widehat{\mathbf{H}}) (\mathbf{I} + \widehat{\mathbf{H}})^{-1} \mathbf{\Gamma}^{1/2}.$$

Therefore, combining the previous sequence of inequalities

$$\alpha \leq 1 + \|\mathbf{\Gamma}^{-1/2} (\mathbf{H} - \widehat{\mathbf{H}}) (\mathbf{I} + \widehat{\mathbf{H}})^{-1} \mathbf{\Gamma}^{1/2}\|_2 \leq 1 + \sqrt{\kappa_2(\mathbf{\Gamma})} \|(\mathbf{H} - \widehat{\mathbf{H}})\|_2.$$

We have used submultiplicativity,  $\|\mathbf{A}^{1/2}\|_2 = \|\mathbf{A}\|_2^{1/2}$  for an SPD matrix, and  $(\mathbf{I} + \widehat{\mathbf{H}})$  is SPD with the eigenvalues bounded from below by 1.

To bound  $\beta$ , we split into two cases:

1. Suppose  $\widehat{\mathbf{H}} \preceq \mathbf{H}$ . Then  $\widehat{\mathbf{H}} \preceq \mathbf{H}$  and  $\widehat{\mathcal{H}} \preceq \mathcal{H}$ . Since  $\mathcal{H}$  is invertible,

$$\mathcal{H}^{-1/2} \widehat{\mathcal{H}} \mathcal{H}^{-1/2} \preceq \mathbf{I}.$$

Since the nonzero eigenvalues of  $\mathbf{A}\mathbf{B}$  are the same as  $\mathbf{B}\mathbf{A}$ , the spectral radius of  $\mathcal{H}^{-1/2} \widehat{\mathcal{H}} \mathcal{H}^{-1/2}$  is the same as  $\widehat{\mathcal{H}}^{1/2} \mathcal{H}^{-1} \widehat{\mathcal{H}}^{1/2}$  and is bounded by 1. This implies  $\beta \leq 1$ .

2. Suppose otherwise, then by the triangle inequality,

$$\beta = \|\mathcal{H}^{-1/2} \widehat{\mathcal{H}} \mathcal{H}^{-1/2}\|_2 = \|\mathbf{I} + \mathcal{H}^{-1/2} (\widehat{\mathcal{H}} - \mathcal{H}) \mathcal{H}^{-1/2}\|_2 \leq 1 + \sqrt{\kappa_2(\mathbf{\Gamma})} \|(\mathbf{H} - \widehat{\mathbf{H}})\|_2.$$

The last step follows a similar derivation as for the case of  $\alpha$ .

We have the desired result by combining the bounds for  $\alpha$  and  $\beta$ .  $\square$

#### 4.4. Probabilistic analysis

In this subsection, we use the structural bounds to derive bounds for the three sketching methods in Section 3.1.

*Proof of Theorem 1.* Compute the sketch  $\mathbf{Y} = \mathbf{A}\mathbf{\Omega}$  and the thin QR factorization  $\mathbf{Y} = \mathbf{Q}\mathbf{R}$ . The low-rank approximation is  $\widehat{\mathbf{H}} = \mathbf{A}^\top \mathbf{Q}\mathbf{Q}^\top \mathbf{A} = \widehat{\mathbf{V}} \widehat{\mathbf{\Lambda}} \widehat{\mathbf{V}}^\top$ . We tackle each part individually.

Part 1. By Theorem 4, the error in the solution depends only on the error in the low-rank approximation  $\|\mathbf{H} - \widehat{\mathbf{H}}\|_2$ . Using the fact that the orthogonal projector is symmetric and idempotent, we can rewrite this as

$$\|\mathbf{H} - \widehat{\mathbf{H}}\|_2 = \|\mathbf{A}^\top (\mathbf{I} - \mathbf{Q}\mathbf{Q}^\top) \mathbf{A}\|_2 = \|(\mathbf{I} - \mathbf{Q}\mathbf{Q}^\top) \mathbf{A}\|_2^2.$$

Since  $\mathcal{R}(\mathbf{Y}) \subset \mathcal{R}(\mathbf{Q})$ , by [20, Proposition 8.5],

$$\|(\mathbf{I} - \mathbf{Q}\mathbf{Q}^\top) \mathbf{A}\|_2^2 \leq \|(\mathbf{I} - \mathbf{Y}\mathbf{Y}^\dagger) \mathbf{A}\|_2^2 \leq \|\mathbf{\Sigma}_2\|_2^2 + \|\mathbf{\Sigma}_2 \mathbf{\Omega}_2 \mathbf{\Omega}_1^\dagger\|_2^2,$$

where  $\mathbf{\Omega}_1 = \mathbf{V}_1^\top \mathbf{\Omega}$  and  $\mathbf{\Omega}_2 = \mathbf{V}_2^\top \mathbf{\Omega}$ . Taking expectations and using the fact that the spectral norm is dominated by the Frobenius norm

$$\mathbb{E} \left[ \|\mathbf{H} - \widehat{\mathbf{H}}\|_2 \right] \leq \|\mathbf{\Sigma}_2\|_2^2 + \mathbb{E} \left[ \|\mathbf{\Sigma}_2 \mathbf{\Omega}_2 \mathbf{\Omega}_1^\dagger\|_F^2 \right].$$

From the proof of [20, Theorem 10.5],  $\mathbb{E} \left[ \|\mathbf{\Sigma}_2 \mathbf{\Omega}_2 \mathbf{\Omega}_1^\dagger\|_F^2 \right] \leq \frac{r}{p-1} \|\mathbf{\Sigma}_2\|_F^2$ . Plug the inequality into the above bound, and identify the singular values with the eigenvalues.

Part 3. Since  $\mathbf{Q}\mathbf{Q}^\top \preceq \mathbf{I}$ ,  $\widehat{\mathbf{H}} \preceq \mathbf{H}$ . Therefore, Theorem 6 applies. The rest of the proof is similar to parts 1-2.  $\square$

*Proof of Theorem 2.* As before, we tackle each part separately.

Part 1. Follows from Theorem 4 and [24, Theorem 14.1]. Part 2. First, observe that

$$\widehat{\mathbf{H}} = \mathbf{Y}(\mathbf{\Omega}^\top \mathbf{Y})^\dagger \mathbf{Y}^\top = \mathbf{H}\mathbf{\Omega}(\mathbf{\Omega}^\top \mathbf{H}\mathbf{\Omega})^\dagger \mathbf{H}\mathbf{\Omega}^\top = \mathbf{H}^{1/2} \mathbf{P}_{\mathbf{H}^{1/2}\mathbf{\Omega}} \mathbf{H}^{1/2},$$

where  $\mathbf{P}_{\mathbf{H}^{1/2}\mathbf{\Omega}} = \mathbf{H}^{1/2} \mathbf{\Omega}(\mathbf{\Omega}^\top \mathbf{H}\mathbf{\Omega})^\dagger \mathbf{\Omega}^\top \mathbf{H}^{1/2}$  is an orthogonal projector. This means  $\mathbf{P}_{\mathbf{H}^{1/2}\mathbf{\Omega}} \preceq \mathbf{I}$  and  $\widehat{\mathbf{H}} \preceq \mathbf{H}$ . Therefore, the second part of Theorem 6 applies and

$$\mathbb{E} \left[ \kappa_2(\widehat{\mathcal{H}}^{-1/2} \mathcal{H} \widehat{\mathcal{H}}^{-1/2}) \right] \leq 1 + \mathbb{E} \left[ \sqrt{\kappa_2(\mathbf{\Gamma})} \|\mathbf{H} - \widehat{\mathbf{H}}\|_2 \right].$$

The proof then follows from [24, Theorem 14.1].

Part 3. This is similar to Part 1 but uses Theorem 5 instead.  $\square$

*Proof of Theorem 3.* To prove this theorem, we first recognize that  $\mathbf{E} = \mathbf{H} - \widehat{\mathbf{H}}$  is no longer positive semidefinite, so we have to use the weaker result in Theorem 6.

Part 1. By Theorem 4, the error in the solution depends only on the error in the low-rank approximation  $\|\mathbf{E}\|_2$ . Using triangle inequality and submultiplicativity

$$\begin{aligned} \|\mathbf{H} - \widehat{\mathbf{H}}\|_2 &= \|\mathbf{A}^\top \mathbf{A} - \mathbf{A}^\top \widehat{\mathbf{A}} + \mathbf{A}^\top \widehat{\mathbf{A}} - \widehat{\mathbf{A}}^\top \widehat{\mathbf{A}}\|_2 \\ &\leq \|\mathbf{A}\|_2 \|\mathbf{A} - \widehat{\mathbf{A}}\|_2 + \|\mathbf{A} - \widehat{\mathbf{A}}\|_2 \|\widehat{\mathbf{A}}\|_2. \end{aligned}$$

Write  $\widehat{\mathbf{A}} = \widehat{\mathbf{A}} - \mathbf{A} + \mathbf{A}$ , and once again apply triangle inequality to get

$$\|\mathbf{H} - \widehat{\mathbf{H}}\|_2 \leq 2\|\mathbf{A}\|_2 \|\mathbf{A} - \widehat{\mathbf{A}}\|_2 + \|\mathbf{A} - \widehat{\mathbf{A}}\|_2^2.$$

The spectral norm is bounded by the Frobenius norm. Take expectations and apply Cauchy-Schwartz inequality to get

$$\mathbb{E} \left[ \|\mathbf{H} - \widehat{\mathbf{H}}\|_2 \right] \leq 2\|\mathbf{A}\|_2 \left( \mathbb{E} \left[ \|\mathbf{A} - \widehat{\mathbf{A}}\|_F^2 \right] \right)^{1/2} + \mathbb{E} \left[ \|\mathbf{A} - \widehat{\mathbf{A}}\|_F^2 \right]. \quad (23)$$

By [42, Theorem 4.3],

$$\mathbb{E} \left[ \|\mathbf{A} - \widehat{\mathbf{A}}\|_F^2 \right] \leq (1 + f(\ell_1, \ell_2))(1 + f(r, \ell_1)) \sum_{j>r} \sigma_j^2,$$

where  $f(a, b) = a/(b - a - 1)$ . Take  $\ell_1 = 2r + 1$ , and  $\ell_2 = 2\ell_1 + 1$  so that  $f(r, \ell_1) = f(\ell_1, \ell_2) = \frac{3}{2}$ .

This gives  $\mathbb{E} \left[ \|\mathbf{A} - \widehat{\mathbf{A}}\|_F^2 \right] \leq \frac{9}{4} \sum_{j>r} \sigma_j^2$ . Plug into eq. (23) and simplify.

Part 2: By Theorem 6,

$$\sqrt{\kappa_2(\widehat{\mathcal{H}}^{-1/2}\mathcal{H}\widehat{\mathcal{H}}^{-1/2})} \leq 1 + \sqrt{\kappa_2(\mathbf{\Gamma})}\|\mathbf{H} - \widehat{\mathbf{H}}\|_2.$$

The rest of the proof is similar to Part 1.

Part 3: The proof is similar to Part 1, but uses Theorem 5.  $\square$

## 5. Numerical Experiments

This section describes experiments on two different PDEs, namely (i) the 1-D Burgers equation, and (ii) barotropic vorticity equation. MATLAB 2023a was used to perform the numerical experiments. We use a custom Gauss-Newton solver with the Moré-Thuente line search [25] from POBLANO [11]. The settings for each experiment are detailed in the corresponding subsections and summarized in Table 2 respectively. We define the relative error of the analysis trajectory

Setting	Application 1	Application 2
Domain	$x \in (0, 1)$	$(x, y) \in (0, 1) \times (-1, 1)$
Parameters	$\nu \in \{10^{-3}, 10^{-2}, 10^{-1}, 1\}$	$\text{Re} = 200, \text{Ro} = 0.0016$
State size	$n \in \{199, 399, 599, 799\}$	$n = 128 \times 257 = 32896$
$\Delta t$	0.01	0.001225 (around 6 hours)
$n_t$	20	8
$n_{\text{obs}}$	15	256
$\mathbf{\Gamma}$	$(0.5\mathbf{I} - 500\mathbf{\Delta}^*)^{-2}$	$(-0.06\mathbf{\Delta}^*)^{-2}$
$\mathbf{R}_i, 1 \leq i \leq n_t$	$0.01 \cdot \mathbf{I}_{15}$	$361 \cdot \mathbf{I}_{256}$
$\ \nabla \mathcal{J}\ _2$ tolerance	$n \cdot 10^{-6}$	$n \cdot 10^{-5}$
PCG tolerance	$10^{-10}$	$10^{-6}$
Max PCG iterations	1000	1000

Table 2: Summary of experiment settings.  $\mathbf{\Delta}^*$  refers to the discrete Laplacian operator with Dirichlet boundary conditions: the 3-point and 5-point stencil for Experiments 1 and 2 respectively.

as

$$\frac{\|\mathbf{x}_i^a - \mathbf{x}_i^{\text{true}}\|_2}{\|\mathbf{x}_i^{\text{true}}\|_2} \quad 0 \leq i \leq n_k, \quad (24)$$

at each time instance  $n_k \Delta t$ . Here,  $\mathbf{x}_i^a$  is the analysis  $\mathbf{x}_0^a$  forecasted to time  $t_i$ ,  $\mathbf{x}_i^{\text{true}}$  is the true solution at  $t_i$ , and  $n_k$  is a discrete number of time instances we compare the two values.

Note that we choose  $n_k > n_t$ , meaning we consider the forecasting potential of the  $\mathbf{x}_0^a$  without any observations after the observation time window has elapsed. For the test problems in Experiments 1.1 and 2, we report (i) the total number of PCG iterations that are required to obtain the solution of the SC-4DVAR optimization problem, (ii) the total number of parallelizable (or offline) TLM  $\mathbf{A}$  and ADJ  $\mathbf{A}^\top$  solutions that are required to create sketches (SketchSolv or SketchPrec) across the full optimization, (iii) the total number of sequential (or online) TLM and ADJ solves used in the computation of the gradient (SketchSolv and SketchPrec), GN Hessian (SketchPrec only), and (iv) the total number of PDE solves including those done inside the line-search.

### 5.1. Application 1: 1-D Burgers' Equation

The first application we consider is the non-linear, one-dimensional viscous Burgers' equation. This equation describes the non-linear advection and diffusion of a fluid in space and time. Some of the problem settings are inspired by the advection-diffusion example from [17]. Consider the PDE

$$\frac{\partial u}{\partial t} + u \frac{\partial u}{\partial x} = \nu \frac{\partial^2 u}{\partial x^2}, \quad (25)$$

with domain  $x \in (0, 1)$ , diffusion coefficient  $\nu = 0.1$ , and homogeneous Dirichlet boundary conditions  $u(t, 0) = u(t, 1) = 0$ . The spatial derivatives are computed using second-order central finite differences on a uniform mesh. The time stepping uses a 3rd-order, explicit, total variation diminishing Runge Kutta [19] scheme (called RK3). For Experiments 1.1 and 1.2, we use the grid size  $n = 399$  giving  $\Delta x = 0.0025$ , and for Experiments 1.3 and 1.4, we use  $n \in \{199, 399, 599, 799\}$ . For Experiments 1.1 and 1.2, the RK3 timestep  $\Delta t_{ts} = 2.5 \times 10^{-5}$ . For experiments 1.3 and 1.4,  $\Delta t_{ts}$  is chosen sufficiently small based on problem settings to have stable solutions. The discrete Runge Kutta TLM and ADJ [35] are used to compute the gradients and Hessian vector products.

*Data and Background.* For all experiments, the true initial condition  $\mathbf{x}_0^{\text{true}}$  is set based on the discrete representation of  $\sin(\pi x)$ . In standard SC-4DVAR fashion [13, 17, 4, 10], the background estimate is chosen by adding a background scaled perturbation to the true initial condition as  $\mathbf{x}_0^b = \mathbf{x}_0^{\text{true}} + \mathbf{\Gamma}^{\frac{1}{2}} \boldsymbol{\xi}$ , with the covariance matrix  $\mathbf{\Gamma} = (0.5\mathbf{I} - 500\mathbf{\Delta}^*)^{-2}$  where  $\mathbf{\Delta}^*$  is the discrete Laplacian with homogeneous Dirichlet boundary conditions and  $\boldsymbol{\xi} \sim \mathcal{N}(\mathbf{0}, \mathbf{I})$ . The parameters of the covariance  $\mathbf{\Gamma}$  are obtained by hand-tuning.

Observations are recorded for a window of  $n_t = 20$  time instances, each instance separated by an interval of  $\Delta t = 0.01$  time units. For all experiments (1.1 through to 1.4), we observe 15 states at the x-intercepts of the observations shown in fig. 2. The observation error for all experiments (1.1 through to 1.4) is  $\mathbf{R}_i = 0.01 \cdot \mathbf{I}_{15}$  for  $1 \leq i \leq n_t$ . Figure 2 shows an example of the true solution, observations at the locations, and a background estimate.

*Optimization and PCG settings.* The optimizer for every variant of the GN method is terminated when the norm of the gradient decreases below a specified tolerance (here, when  $\|\nabla \mathcal{J}\|_2 < n \cdot 10^{-6}$ ). The optimization is initialized with the background  $\mathbf{x}_0^{(0)} = \mathbf{x}_0^b$ . PCG for computing the descent direction is terminated when the relative residual of the  $k$ -th iterate achieves a prespecified tolerance (here  $10^{-10}$ , with a maximum of 1000 PCG iterations). In numerical experiments, we observe that without a preconditioner, PCG failed to converge within 1000 iterations, and therefore, we do not report this result. The base case for GN (called Std GN), uses the background covariance matrix  $\mathbf{\Gamma}$  as a preconditioner.

#### 5.1.1. Experiment 1.1: Comparing the sketching approaches

In this experiment, we compare all the proposed sketching methods—RandSVD, Nyström, SingleView—and the optimization techniques—SketchSolv, SketchPrec—in terms of the relative analysis trajectory error as defined in eq. (24) with  $n_k = 81$ . The sketch sizes are  $\ell = 15$  for RandSVD and Nyström, and  $\ell_1 = 15, \ell_2 = 31$  for SingleView. The preconditioners are updated at each GN iteration; we explore the adaptive approach in the second application.

Figure 3a shows that all the variants of the GN method have the same relative analysis trajectory error, which is lower than the forecast error (whose trajectory is obtained by evolving the background without any assimilation). The relative error difference between the analysis

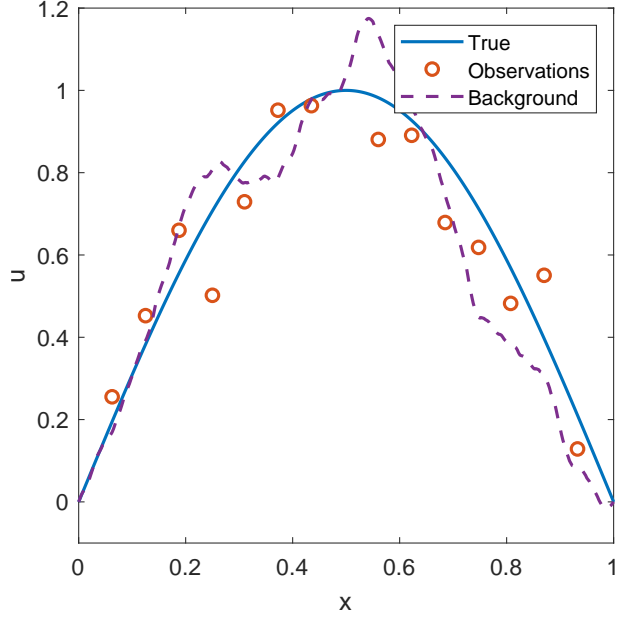


Figure 2: An illustration depicting the true states, its noisy observation at time 0, and a background estimate.

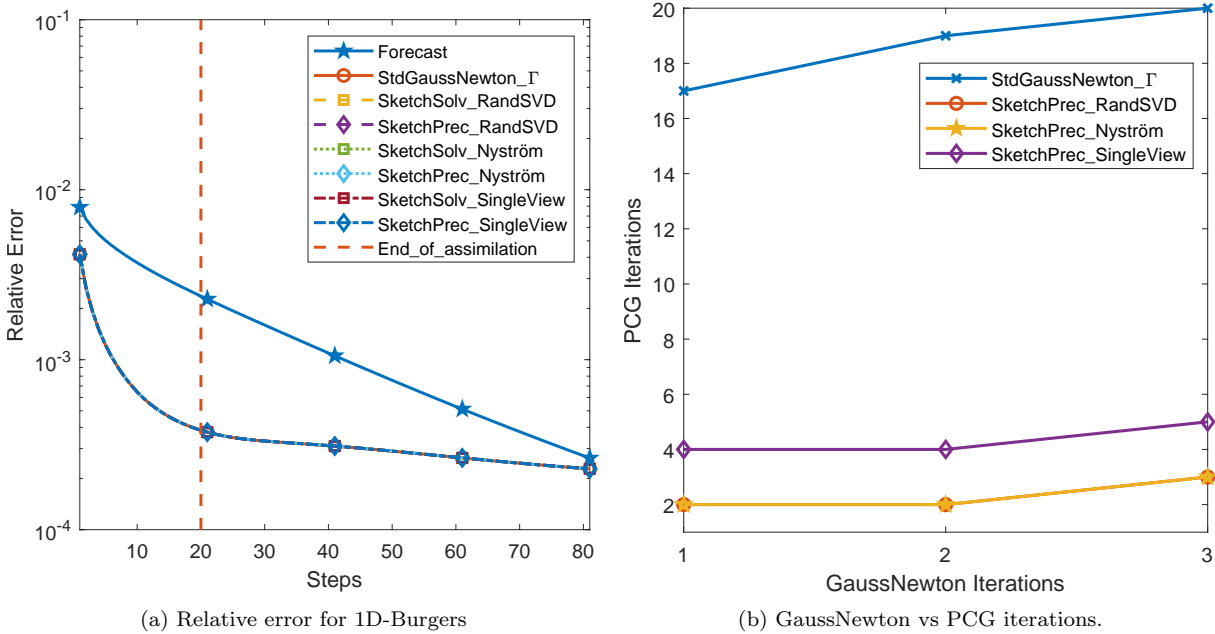


Figure 3: The relative error in Figure 3a has similar behavior in time across the different methods. Figure 3b shows a decrease in the number of PCG iterations for the preconditioned methods.

trajectory and background becomes smaller over time, due to the highly diffusive nature of the problem. Figure 3b shows the total number of PCG iterations for the approaches. As expected, the randomized preconditioned approaches require fewer CG iterations compared to Std GN, and we also observe similar behavior across the randomized methods. Table 3 provides a more quantitative picture of the full cost of sketching. Both SketchSolv and SketchPrec, outsource a major portion of the computations into the offline section ( $\sim 88\%$ ), and the total PCG iterations

Precond.	#PCG	Par/Offline/Setup		Seq/Online			Total	
	Iterations	#TLM	#ADJ	#FWD	#TLM	#ADJ	#TLM	#ADJ
Std GN								
$\Gamma$	56	—	—	4	56	59	56	59
SketchPrec								
RandSVD	6	45	45	8	6	9	51	54
Nyström	6	45	45	8	6	9	51	54
SingleView	13	45	63	8	13	16	58	79
SketchSolv								
RandSVD	0	45	45	4	0	3	45	48
Nyström	0	45	45	4	0	3	45	48
SingleView	0	45	63	4	0	3	45	66

Table 3: Summary of the comparison of proposed methods for the 1-D Burgers equation. All methods take 3 GN iterations. The sketch parameters are  $\ell = \ell_1 = 15$  and  $\ell_2 = 31$ .

in SketchPrec have been drastically reduced. A noteworthy observation is that the randomized methods are robust to changes in the seed for the random number generator. If we compare the sketching methods in Table 3, RandSVD and Nyström sketches have similar behavior for both SketchSolv and SketchPrec while SingleView is slightly more expensive to construct and requires more iterations, but, at the same time, has a higher potential for parallelism.

### 5.1.2. Experiment 1.2: Condition Numbers and PCG iterations

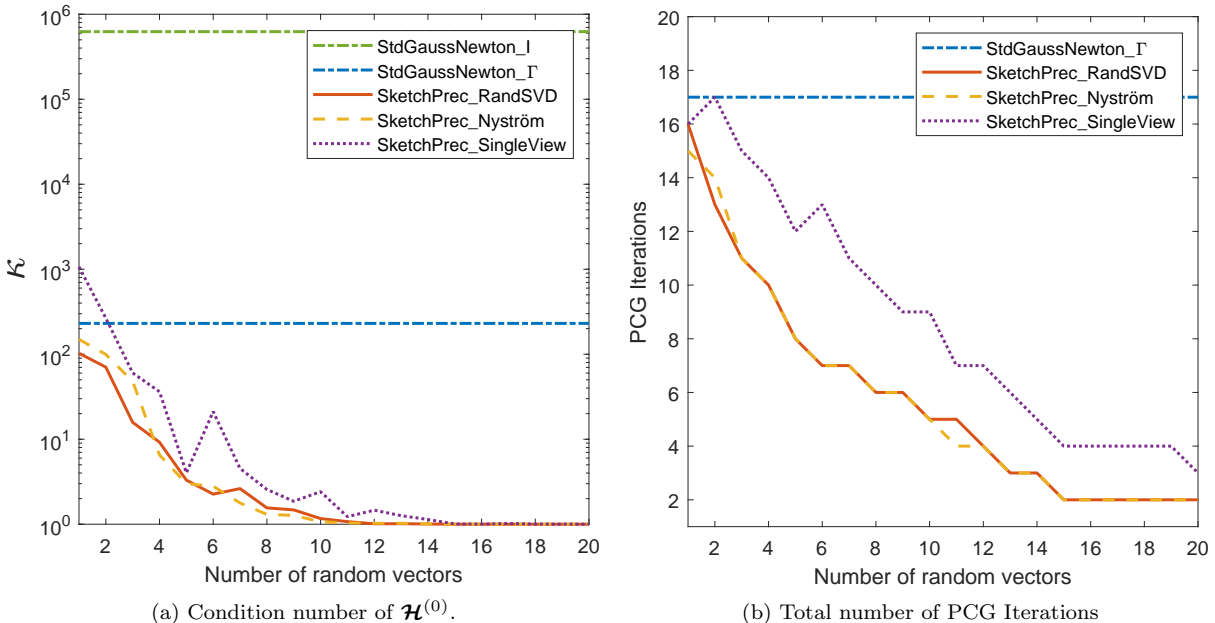


Figure 4: Influence of the sketch size on the preconditioning of GN Hessian on the first GN iteration. The sketch size here refers to  $\ell$  (RandSVD and Nyström) and  $\ell_1$  (SingleView).

We retain the problem settings of Experiment 1, varying only the sketch sizes  $\ell$  (RandSVD, Nyström) and  $\ell_1$  (SingleView), with  $\ell_2$  constrained as  $\ell_2 = 2\ell_1 + 1$ . The idea is to test the effect

of changing the sketch sizes  $\ell$ , and  $\ell_1$  on the conditioning of  $\mathcal{H}^{(0)}(\mathbf{x}_0^{(0)}) = \mathcal{H}^{(0)}(\mathbf{x}_0^b)$  (the first iterate of the GN Hessian as in eq. (10), and the total number of PCG iterations to solve the system  $\mathcal{H}^{(0)}(\mathbf{x}_0^b)\delta\mathbf{x}^{(0)} = -\mathbf{g}^{(0)}(\mathbf{x}_0^b)$ .

In Figure 4a we observe that a larger sketch size results in a better condition number and that the condition number is much lower than without a preconditioner and with  $\mathbf{\Gamma}$  as the preconditioner. As expected from the theory in Section 4, using a larger sketch size to construct the preconditioners improves the conditioning of the system. In particular, For the sketch sizes  $\ell = 13$  (RandSVD and Nyström) and  $\ell_1 = 18$  (SingleView), the condition number of the preconditioned operator is very close to 1, implying rapid PCG convergence.

To explain these observations, let us consider the notation in Section 4. The GN Hessian is  $\mathcal{H} = \mathbf{\Gamma}^{-1/2}(\mathbf{I} + \mathbf{H})\mathbf{\Gamma}^{-1/2}$  (the index 0 has been dropped) with eigenvalues of  $\mathbf{H}$  denoted  $\lambda_1 \geq \dots \lambda_n \geq 0$ . Furthermore, consider Std GN with  $\mathbf{\Gamma}$  as the preconditioner (i.e.,  $\widehat{\mathcal{H}} = \mathbf{\Gamma}$ ) and assume  $m \leq n$  so that  $\lambda_n(\mathcal{H}) = 0$ . Then  $\kappa_2(\mathbf{\Gamma}^{1/2}\mathcal{H}\mathbf{\Gamma}^{1/2}) = 1 + \lambda_1$ . If, instead, the identity matrix is used as a preconditioner,  $\widehat{\mathcal{H}} = \mathbf{I}$ , then we have the bound  $\kappa_2(\mathcal{H}) \leq \kappa_2(\mathbf{\Gamma})(1 + \lambda_1)$ . In contrast, for RandSVD, Theorem 1 says that

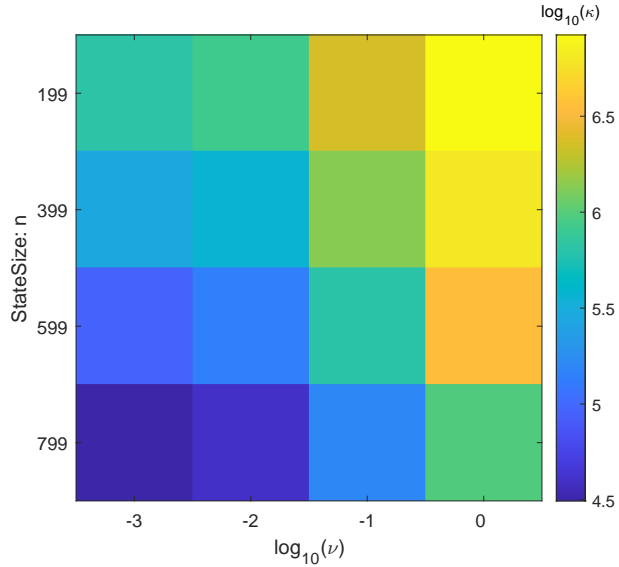
$$\mathbb{E} \left[ \kappa_2(\widehat{\mathcal{H}}^{-1/2}\mathcal{H}\widehat{\mathcal{H}}^{-1/2}) \right] \leq 1 + \sqrt{\kappa_2(\mathbf{\Gamma})} \left( 1 + \frac{r}{p-1} \text{id}_r \right) \lambda_{r+1}. \quad (26)$$

Therefore,  $\kappa_2(\widehat{\mathcal{H}}^{-1/2}\mathcal{H}\widehat{\mathcal{H}}^{-1/2})$  can be much smaller than  $\kappa_2(\mathbf{\Gamma}^{1/2}\mathcal{H}\mathbf{\Gamma}^{1/2})$  provided  $\lambda_{r+1} \ll \lambda_1$  and  $\mathbf{\Gamma}$  is reasonably well-conditioned. Only the first condition is necessary for  $\kappa_2(\widehat{\mathcal{H}}^{-1/2}\mathcal{H}\widehat{\mathcal{H}}^{-1/2})$  to have a smaller upper bound than  $\kappa_2(\mathcal{H})$ . The next experiment gives empirical evidence for the condition  $\lambda_{r+1} \ll \lambda_1$ . Similar observations can be made for Nyström and SingleView. Note that Theorem 3 predicts a larger condition number  $\kappa_2(\widehat{\mathcal{H}}^{-1/2}\mathcal{H}\widehat{\mathcal{H}}^{-1/2})$  and this is observed in experiments as well.

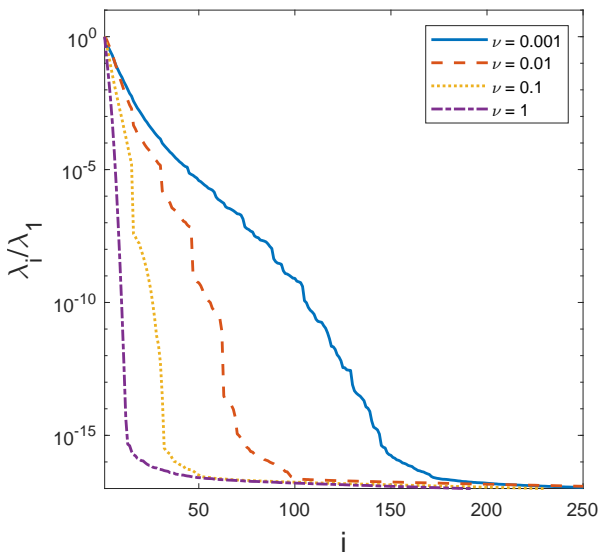
In Figure 4b we see that a larger sketch size results in fewer PCG iterations, and the randomized preconditioners improve on the background covariance as the preconditioner. Without the use of a preconditioner (i.e., using the identity matrix as a preconditioner), we see that PCG does not converge even in a maximum of 1000 iterations and that the condition number of the GN Hessian is high (cf. Figure 4a). Between the different sketching methods, RandSVD and Nyström require slightly smaller sketch sizes, and ultimately fewer TLMs/ADJs, than the SingleView method for convergence.

### 5.1.3. Experiment 1.3: Conditioning of the GN Hessian

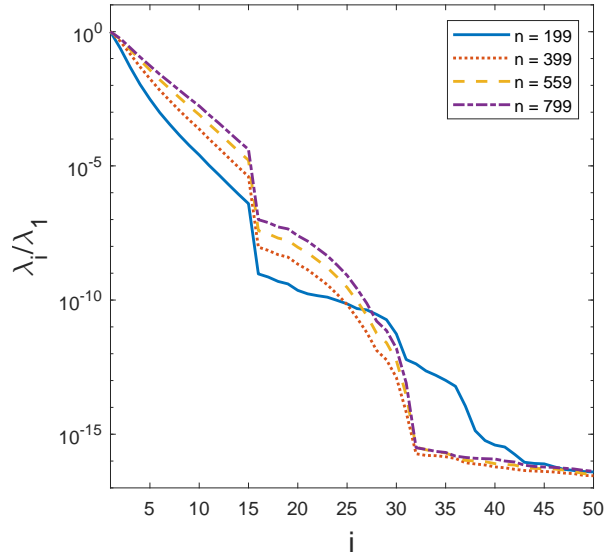
We now look at the condition number of  $\mathcal{H}^{(0)}(\mathbf{x}_0^b)$ , by varying the discretization or state size ( $n$ ) and diffusion coefficient ( $\nu$ ). To ensure consistency across the experiments, the background state  $\mathbf{x}_0^b$  is first computed for the finest grid  $n = 799$ , and its values are interpolated for the other grid sizes  $n \in \{199, 399, 599\}$ . The background covariance chosen as in the previous experiments, produces initial conditions that are smooth enough to behave similarly for all of these discretizations. The observations are collected at the same spatial locations at all discretization levels (matching the observation x-locations in Figure 2) and do not change in value across the experiments. Figure 5a shows the dependence of the condition number of  $\mathcal{H}^{(0)}(\mathbf{x}_0^b)$  on the logarithm of diffusion coefficient  $\nu$  and state size  $n$ . The dependence of the scaled eigenvalues of the regularized data misfit Hessian  $\mathbf{H}$  on  $n$  and  $\nu$  are shown in Figure 5b. We make two observations here:



(a) Condition number of the GN Hessian  $\mathcal{H}^{(0)}(\mathbf{x}_0^b)$  at the initial iterate.



(b) Relative spectral decay  $n = 399$



(c) Relative spectral decay for  $\nu = 0.1$

Figure 5: Conditioning and spectral decay for different settings of the Burgers equation. Here,  $i$  indexes  $\sigma_i$  which is the  $i$ th largest eigenvalue.

1. The eigenvalues show a sharper decay with increased diffusion as seen in Figure 5b, and the condition number increases with smaller diffusion coefficient  $\nu$  (less diffusive) as seen from the rows of Figure 5a.
2. The eigenvalue decay is similar across multiple values of  $n$  as seen in Figure 5c, and the condition number increases with larger grid sizes as seen from the columns of Figure 5a.
3. Experimentally, we see that the eigenvalue decay for systems with  $\nu = 0.01, 0.1, 1$  in Figure 5 is consistent with the spectra of severely ill-posed problems (cf. Section 4.2).

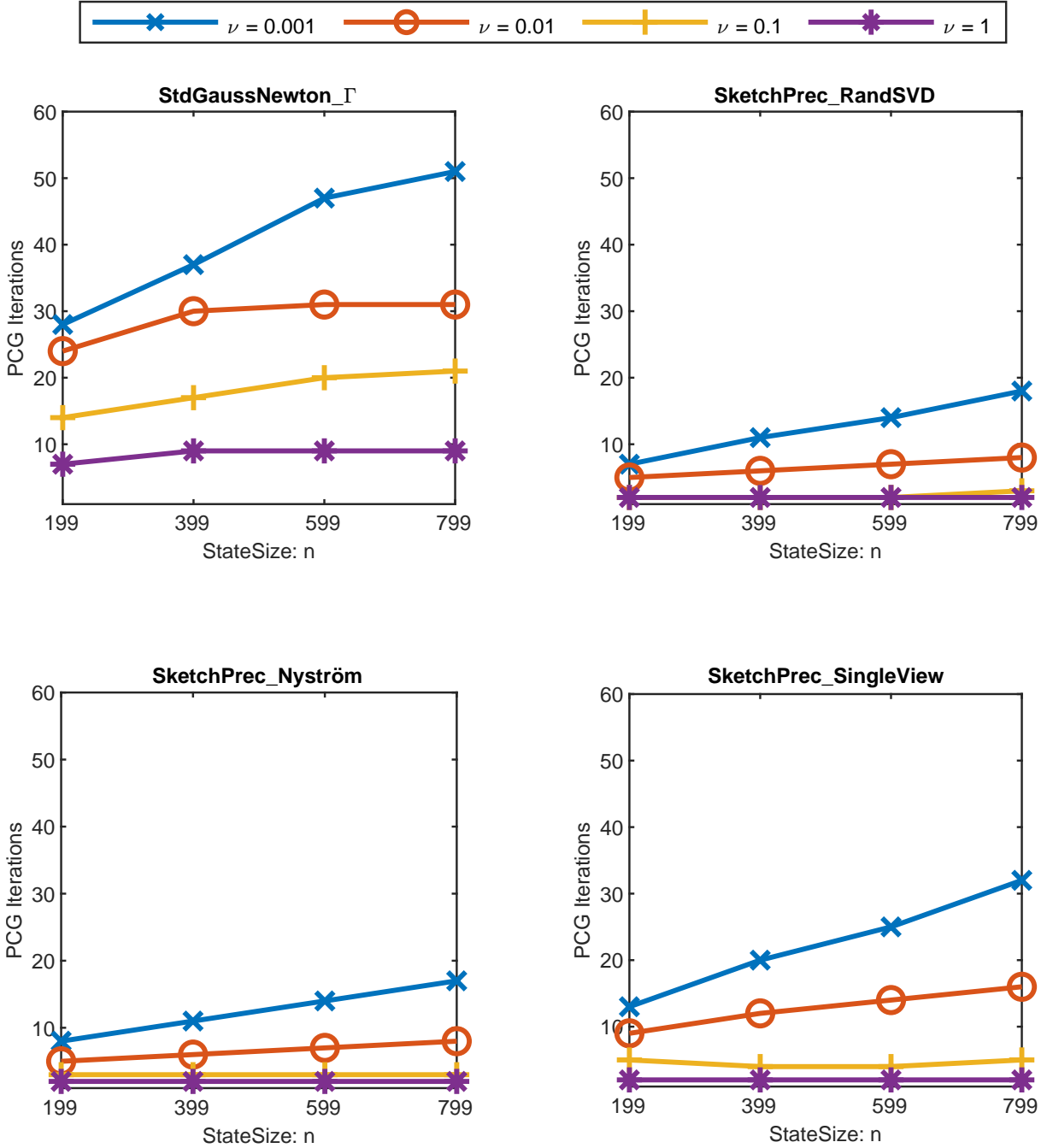


Figure 6: Effective mesh refinement

#### 5.1.4. Experiment 1.4: Effect of mesh refinement

In this experiment, we use the settings of the previous experiment with sketch sizes  $\ell = \ell_1 = 15$  and  $\ell_2 = 2\ell_1 + 1$ . We report the number of PCG iterations to solve for the first descent direction using the background covariance as the preconditioner and with each of the sketched preconditioners in Figure 6. For larger values of the diffusion coefficient  $\nu$  ( $\nu$  in the range 0.1–1), all the approaches do not show a significant change in the number of PCG iterations at different

grid sizes. However, as the diffusion  $\nu$  decreases ( $\nu$  in the range 0.001 – 0.01), the PDE becomes less diffusive, and the number of PCG iterations for all the methods shows a mild increase with increasing grid sizes. Therefore, the preconditioners only have grid-independent behavior for more diffusive regimes and show grid-dependent behavior for less diffusive regimes. In all the cases considered, the sketched preconditioners result in fewer PCG iterations compared to the background covariance as the preconditioner for the same grid size.

### 5.2. Application 2: Barotropic vorticity equation

For the second application, we consider the barotropic vorticity equation which represents a large-scale, turbulent, wind-driven circulation in a shallow oceanic basin [34], that is a typical test problem for data assimilation problem [39, 12, 1, 28]. We follow the non-dimensional formulation as described in [34]:

$$\begin{aligned} \frac{\partial \omega}{\partial t} + \left( \frac{\partial \psi}{\partial y} \frac{\partial \omega}{\partial x} - \frac{\partial \psi}{\partial x} \frac{\partial \omega}{\partial y} \right) - \text{Ro}^{-1} \frac{\partial \psi}{\partial x} &= \text{Re}^{-1} \left( \frac{\partial^2 \omega}{\partial x^2} + \frac{\partial^2 \omega}{\partial y^2} \right) + \text{Ro}^{-1} F, \\ \frac{\partial^2 \psi}{\partial x^2} + \frac{\partial^2 \psi}{\partial y^2} &= -\omega, \end{aligned} \tag{27}$$

where  $(x, y) \in \Omega = (0, 1) \times (-1, 1)$ ,  $\omega$  is the vorticity,  $\psi$  is the stream function,  $\text{Re} = 200$  is the Reynolds number,  $\text{Ro} = 0.0016$  is the Rossby number, and a symmetric double gyre forcing function  $F(x, y) = \sin(\pi y)$  and homogeneous Dirichlet boundary conditions (i.e.,  $\psi|_{\Omega} = \omega|_{\Omega} = 0$ ).

The PDE is spatially discretized on a uniform mesh using second-order central finite differences. We have the number of grid points  $n = 128 \times 257 = 32,896$  with grid spacing  $\Delta x = \Delta y = 0.0078$ . A 3rd-order, explicit, total variation diminishing Runge Kutta [19] scheme is used to evolve the semidiscretized PDE in time with a timestep of  $\Delta t_{ts} = 0.000245$  time units. The discrete Runge Kutta TLM and ADJ [35] are used to compute the gradients and Hessian vector products.

*Data and Background.* The true initial condition is chosen after evolving a random, isotropic initial field through the system; see Figure 7. As standard in SC-4DVAR literature [13, 17, 4, 10], the background estimate is chosen as  $\mathbf{x}_0^b = \mathbf{x}_0^{\text{true}} + \mathbf{\Gamma}^{\frac{1}{2}} \boldsymbol{\xi}$ , where the covariance matrix  $\mathbf{\Gamma} = (-0.06 \mathbf{\Delta}^*)^{-2}$ ,  $\mathbf{\Delta}^*$  is the discrete Laplacian with homogeneous Dirichlet boundary conditions, and  $\boldsymbol{\xi} \sim \mathcal{N}(\mathbf{0}, \mathbf{I})$ . The system is observed every  $\Delta t = 0.001225$  time units (corresponding, roughly, to 6 hours of oceanic flow) for  $n_t = 8$  sequential instances. The data is collected on a sensor network  $16 \times 16$  grid, equally spaced in each dimension as displayed in fig. 7. The observation error covariance is  $\mathbf{R}_i = 361 \cdot \mathbf{I}_{256}$  for  $1 \leq i \leq n_t$  (the parameter is chosen to be around 1 % of the maximum auto-variance.); similarly, the data is corrupted with the observational error drawn from  $\boldsymbol{\epsilon}_i^{\text{obs}} \sim \mathcal{N}(\mathbf{0}, \mathbf{R}_i)$ .

*Optimization and PCG settings.* We only experiment with SketchPrec and do not consider SketchSolv because of the significant computation burden. As before, the optimization is terminated when the norm of the gradient decreases below a specified tolerance (here when  $\|\nabla \mathcal{J}\|_2 < n \cdot 10^{-5}$ ) and initialized with the background  $\mathbf{x}_0^{(0)} = \mathbf{x}_0^b$ . PCG is terminated when the relative residual of the  $k$ -th iterate achieves a prespecified tolerance (here  $10^{-6}$ , with a maximum of 1000 iterations). We compare four sketched preconditioners (RandSVD, Nyström, SingleView, RandSVD\_Adapt) for SketchPrec. For the fixed sketch size case, we take  $\ell = \ell_1 = 384$ , and for

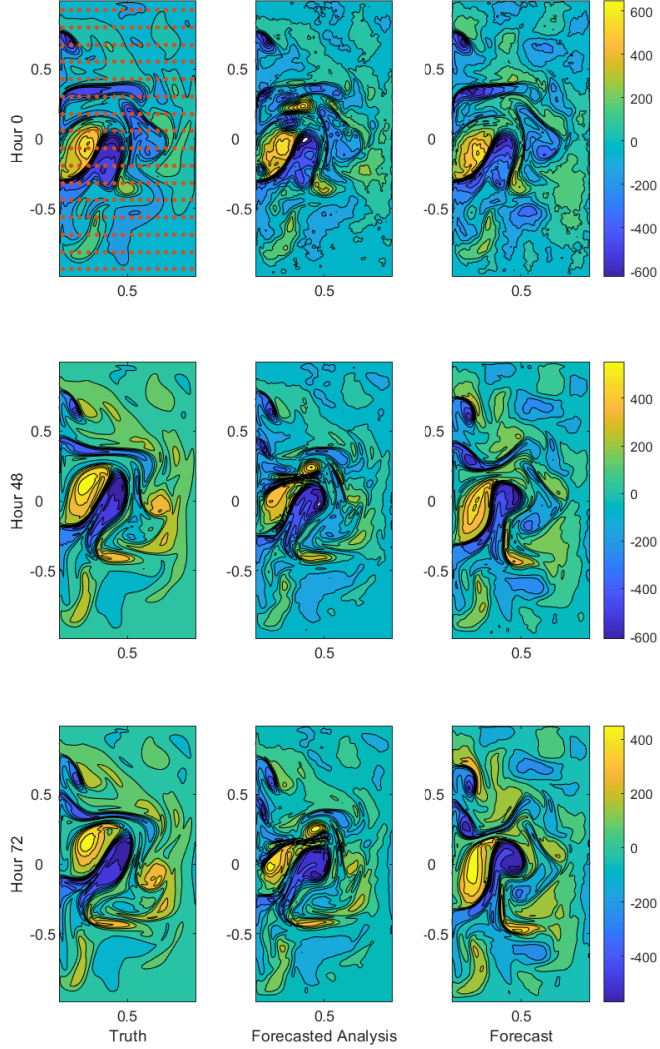


Figure 7: Time snapshots of the true vorticity, forecast, and the forecasted analysis. The assimilation cost considers the data from hour 6 to hour 48. The true data at hour 0 also shows the location of the observation sensors.

the adaptive case, we take  $\epsilon_{re} = 0.65$  and  $\epsilon_{sk} = 0.8$ . In numerical experiments, we observed that without a preconditioner, PCG failed to converge within the maximum number of iterations, and has not been reported. As before, the base case Std GN uses the background covariance matrix  $\mathbf{\Gamma}$  as a preconditioner.

*Results.* Figure 8a shows the relative error over the trajectory for the analyses, and all methods have very similar error trajectories, which are all lower than the forecast trajectory error. Figure 8b compares the PCG iterations required for convergence at each GN step for each of

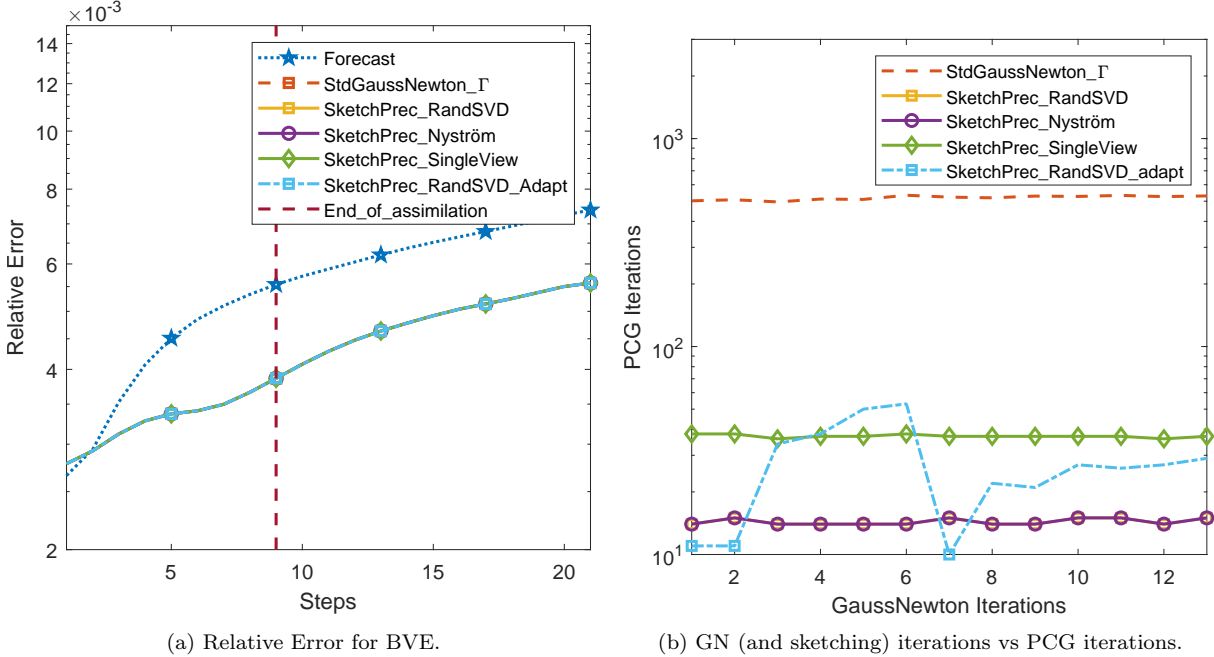


Figure 8: Plots of the relative error and the number of PCG iterations. For the RandSVD\_Adapt, sketches were done for the adaptive only on iterations 1, 2, and 7 (as indicated by markers). The corresponding sketch sizes at all three iterations are 512.

Precond.	#PCG	Par/Offline/Setup		Seq/Online			Total	
	Iterations	#TLM	#ADJ	#FWD	#TLM	#ADJ	#TLM	#ADJ
Std GN								
$\Gamma$	8321	—	—	76	8321	8337	8321	8337
SketchPrec								
RandSVD	231	6144	6144	76	231	247	6375	6391
Nyström	231	6144	6144	76	231	247	6375	6391
SingleView	594	6144	12304	76	594	610	6738	12914
RandSVD_Adapt	452	1536	1536	76	477	493	2013	2029

Table 4: Summary of the numerical results for the BVE. All experiments use 16 outer (GN) iterations. The result for RandSVD\_Adapt also includes the testing cost of computing  $\kappa_{sk}$  and  $\kappa_{re}$ .

the sketching methods. The SketchPrec methods with fixed sketch size—RandSVD, Nyström, and SingleView—all show a large decrease in the total number of PCG iterations compared to Std GN. The fixed sketch size methods are relatively constant in terms of the number of PCG iterations per GN step. Compared to the Std GN method, the RandSVD and Nyström methods reduce the overall number of TLM/ADJ solves by about 23%; in contrast, SingleView was more expensive in terms of ADJ solves. It is worth noting that the bulk of the computations ( $\sim 95\%$ ) involves constructing the preconditioner which can be parallelized.

Focussing on RandSVD\_Adapt, the same figure (Figure 8b) shows that the preconditioner is recomputed at GN iterations 1, 2, and 7. In the remaining GN iterations, the preconditioner is kept fixed. When the preconditioner is recomputed, PCG converges in nearly 10 iterations. The preconditioner computed at GN iteration 2, progressively gets worse across GN iterations

(2 to 6) until it is resketched at GN iteration 7. The preconditioner is updated at GN iteration 7 and is then reused for the remainder of the optimization process. Each time the preconditioner is recomputed, the sketch size was adaptively determined to be 512, based on the parameters  $\epsilon_{\text{re}} = 0.65$  and  $\epsilon_{\text{sk}} = 0.8$ . In terms of the total number of TLMs/ADJs, the RandSVD\_Adapt provides a  $4\times$  speedup compared to Std GN, but as we noted earlier, a substantial portion ( $\sim 75\%$ ) involves offline computations. The RandSVD\_Adapt approach shows a  $3\times$  speedup (in terms of TLM/ADJ applications) compared to fixed sketch size approaches, even accounting for over twice the number of PCG iterations.

## 6. Conclusion and future work

In this paper, we propose new algorithms for solving and preconditioning the SC-4DVAR problem to accelerate the time to solution and reduce total computations. The algorithms are based on different randomized sketching techniques: three methods—RandSVD, Nyström, and SingleView—with fixed sketch size and adaptive approaches to determine when to update the preconditioner and the sketch size. We perform both structural as well as probabilistic analyses of the proposed methods and demonstrate their applicability to several challenging model problems, namely the 1D-Burgers equation and the 2D barotropic vorticity equation. We demonstrate the gains from our preconditioning method in three ways: (i) a substantial reduction in the number of TLM and ADJ solves, (ii) a substantial reduction in the number of PCG iterations, (iii) parallelization of a major portion of the TLM and ADJ solves.

*Future Work.* Randomized approaches to data assimilation have not been effectively used in ensemble data assimilation so far. It would be interesting to explore randomized preconditioners in the context of hybrid ensemble-variational data assimilation methods that are a popular area of research [38].

## 7. Acknowledgements

AKS was supported, in part, by the National Science Foundation through the grant DMS-1845406 and the Department of Energy through the grant DE-SC0023188. Vishwas Rao is supported by the U.S. Department of Energy, Office of Science, Advanced Scientific Computing Research Program under contract DE-AC02-06CH11357. Vishwas Rao thanks Ahmed Attia for helpful discussions.

## References

- [1] M. Ades and P. J. van Leeuwen. The equivalent-weights particle filter in a high-dimensional system. *Quarterly Journal of the Royal Meteorological Society*, 141(687):484–503, 2015.
- [2] M. Asch, M. Bocquet, and M. Nodet. *Data assimilation: methods, algorithms, and applications*. SIAM, 2016.
- [3] R. Bhatia. *Matrix analysis*, volume 169 of *Graduate Texts in Mathematics*. Springer-Verlag, New York, 1997.
- [4] N. Bousserez, J. J. Guerrette, and D. K. Henze. Enhanced parallelization of the incremental 4d-var data assimilation algorithm using the randomized incremental optimal technique. *Quarterly Journal of the Royal Meteorological Society*, 146(728):1351–1371, 2020.

- [5] T. Bui-Thanh, O. Ghattas, J. Martin, and G. Stadler. A computational framework for infinite-dimensional Bayesian inverse problems part i: The linearized case, with application to global seismic inversion. *SIAM Journal on Scientific Computing*, 35(6):A2494–A2523, 2013.
- [6] P. Chen. Hessian matrix vs. Gauss–Newton Hessian matrix. *SIAM Journal on Numerical Analysis*, 49(4):1417–1435, 2011.
- [7] A. Cioaca, M. Alexe, and A. Sandu. Second-order adjoints for solving pde-constrained optimization problems. *Optimization methods and software*, 27(4-5):625–653, 2012.
- [8] T. Cui, J. Martin, Y. M. Marzouk, A. Solonen, and A. Spantini. Likelihood-informed dimension reduction for nonlinear inverse problems. *Inverse Problems*, 30(11):114015, 2014.
- [9] I. Daužickaitė, A. S. Lawless, J. A. Scott, and P. J. van Leeuwen. On time-parallel preconditioning for the state formulation of incremental weak constraint 4D-Var. *Quarterly Journal of the Royal Meteorological Society*, 147(740):3521–3529, 2021.
- [10] I. Daužickaitė, A. S. Lawless, J. A. Scott, and P. J. Van Leeuwen. Randomised preconditioning for the forcing formulation of weak-constraint 4D-Var. *Quarterly Journal of the Royal Meteorological Society*, 147(740):3719–3734, 2021.
- [11] D. M. Dunlavy, E. Acar, and T. G. Kolda. Poblano v1. 0: a MATLAB toolbox for gradient-based optimization. Technical report, Sandia National Laboratories (SNL), Albuquerque, NM, and Livermore, CA, 2010.
- [12] G. Evensen. Sequential data assimilation with a nonlinear quasi-geostrophic model using Monte Carlo methods to forecast error statistics. *Journal of Geophysical Research: Oceans*, 99(C5):10143–10162, 1994.
- [13] G. Evensen, F. C. Vossepoel, and P. J. van Leeuwen. *Data assimilation fundamentals: A unified formulation of the state and parameter estimation problem*. Springer Nature, 2022.
- [14] H. P. Flath, L. C. Wilcox, V. Akçelik, J. Hill, B. van Bloemen Waanders, and O. Ghattas. Fast algorithms for Bayesian uncertainty quantification in large-scale linear inverse problems based on low-rank partial Hessian approximations. *SIAM Journal on Scientific Computing*, 33(1):407–432, 2011.
- [15] Z. Frangella, J. A. Tropp, and M. Udell. Randomized Nyström preconditioning. *SIAM Journal on Matrix Analysis and Applications*, 44(2):718–752, 2023.
- [16] M. A. Freitag. Numerical linear algebra in data assimilation. *GAMM-Mitteilungen*, 43(3):e202000014, 2020.
- [17] M. A. Freitag and D. L. Green. A low-rank approach to the solution of weak constraint variational data assimilation problems. *Journal of Computational Physics*, 357:263–281, 2018.
- [18] M. J. Gander. 50 years of time parallel time integration. In T. Carraro, M. Geiger, S. Körkel, and R. Rannacher, editors, *Multiple Shooting and Time Domain Decomposition Methods*, pages 69–113, Cham, 2015. Springer International Publishing.

- [19] S. Gottlieb and C.-W. Shu. Total variation diminishing Runge-Kutta schemes. *Mathematics of computation*, 67(221):73–85, 1998.
- [20] N. Halko, P.-G. Martinsson, and J. A. Tropp. Finding structure with randomness: Probabilistic algorithms for constructing approximate matrix decompositions. *SIAM review*, 53(2):217–288, 2011.
- [21] P. C. Hansen. *Rank-deficient and discrete ill-posed problems: numerical aspects of linear inversion*. SIAM, 1998.
- [22] E. Kalnay. *Atmospheric Modeling, Data Assimilation and Predictability*. Cambridge University Press, 2003.
- [23] F. Le Dimet and O. Talagrand. Variational algorithms for analysis and assimilation of meteorological observations: theoretical aspects. *Tellus A*, 38(2):97–110, 1986.
- [24] P.-G. Martinsson and J. A. Tropp. Randomized numerical linear algebra: Foundations and algorithms. *Acta Numerica*, 29:403–572, 2020.
- [25] J. J. Moré and D. J. Thuente. Line search algorithms with guaranteed sufficient decrease. *ACM Transactions on Mathematical Software (TOMS)*, 20(3):286–307, 1994.
- [26] A. Nemirovski, A. Juditsky, G. Lan, and A. Shapiro. Robust stochastic approximation approach to stochastic programming. *SIAM Journal on Optimization*, 19(4):1574–1609, 2009.
- [27] J. Nocedal and S. J. Wright. *Numerical optimization*. Springer, 1999.
- [28] A. A. Popov, C. Mou, A. Sandu, and T. Iliescu. A multifidelity ensemble Kalman filter with reduced order control variates. *SIAM Journal on Scientific Computing*, 43(2):A1134–A1162, 2021.
- [29] V. Rao and A. Sandu. An adjoint-based scalable algorithm for time-parallel integration. *Journal of Computational Science*, 5(2):76–84, 2014. Empowering Science through Computing + BioInspired Computing.
- [30] W. Reese, A. K. Saibaba, and J. Lee. Bayesian level set approach for inverse problems with piecewise constant reconstructions. *arXiv preprint arXiv:2111.15620*, 2021.
- [31] Y. Saad. *Iterative methods for sparse linear systems*. SIAM, 2003.
- [32] A. K. Saibaba and P. K. Kitanidis. Fast computation of uncertainty quantification measures in the geostatistical approach to solve inverse problems. *Advances in water resources*, 82:124–138, 2015.
- [33] A. K. Saibaba, P. Prasad, E. De Sturler, E. Miller, and M. E. Kilmer. Randomized approaches to accelerate MCMC algorithms for Bayesian inverse problems. *Journal of Computational Physics*, 440:110391, 2021.
- [34] O. San, A. E. Staples, Z. Wang, and T. Iliescu. Approximate deconvolution large eddy simulation of a barotropic ocean circulation model. *Ocean Modelling*, 40(2):120–132, 2011.

- [35] A. Sandu. On the properties of Runge-Kutta discrete adjoints. In *LNCS 3994*, volume IV(3994), pages 550–557. ICCS 2006, Springer-Verlag Berlin Heidelberg, 2006.
- [36] A. Sandu, D. N. Daescu, G. R. Carmichael, and T. Chai. Adjoint sensitivity analysis of regional air quality models. *Journal of Computational Physics*, 204(1):222–252, 2005.
- [37] A. Spantini, A. Solonen, T. Cui, J. Martin, L. Tenorio, and Y. Marzouk. Optimal low-rank approximations of Bayesian linear inverse problems. *SIAM Journal on Scientific Computing*, 37(6):A2451–A2487, 2015.
- [38] A. N. Subrahmanya, A. A. Popov, and A. Sandu. Ensemble Variational Fokker-Planck Methods for Data Assimilation, 2023.
- [39] O. Talagrand and P. Courtier. Variational assimilation of meteorological observations with the adjoint vorticity equation. Part I: Theory. *Quarterly Journal of the Royal Meteorological Society*, 113:1311–1328, 1987.
- [40] L. N. Trefethen and D. Bau, III. *Numerical linear algebra*. Society for Industrial and Applied Mathematics (SIAM), Philadelphia, PA, 1997.
- [41] J. A. Tropp, A. Yurtsever, M. Udell, and V. Cevher. Fixed-rank approximation of a positive-semidefinite matrix from streaming data. *Advances in Neural Information Processing Systems*, 30, 2017.
- [42] J. A. Tropp, A. Yurtsever, M. Udell, and V. Cevher. Practical sketching algorithms for low-rank matrix approximation. *SIAM Journal on Matrix Analysis and Applications*, 38(4):1454–1485, 2017.
- [43] U. Villa, N. Petra, and O. Ghattas. HIPPYlib: an extensible software framework for large-scale inverse problems governed by PDEs: part i: deterministic inversion and linearized Bayesian inference. *ACM Transactions on Mathematical Software (TOMS)*, 47(2):1–34, 2021.